Experimental and numerical investigation on the effectiveness of NSM and side-NSM CFRP bars for strengthening continuous two-span RC beams

Mohammad Abdallah, Firas Al Mahmoud, M. Idriss Tabet-Derraz, Abdelouahab Khelil, Julien Mercier

Version of Record: https://www.sciencedirect.com/science/article/pii/S2352710221005817
Manuscript_8c38763224a7b50e8e32cd5482c32091

Experimental and numerical investigation on the effectiveness of NSM and side-NSM CFRP bars for strengthening continuous two-span RC beams

Mohammad Abdallah*[1], Firas Al Mahmoud[1], M. Idriss Tabet-Derraz [1,2], Abdelouahab Khelil [1] and Julien Mercier [3]

[1]*Institut Jean Lamour, UMR 7198, CNRS, Université de Lorraine, Nancy, France*

[2]*EOLE laboratory, Department of Civil Engineering, Faculty of Technology, University of Tlemcen, Algeria*

[3]*Freyssinet, Paris, France*

**corresponding author: Mohammad Abdallah, E-mail mohammad.abdallah@univ-lorraine.fr*

Abstract. This paper aims to present and analyze the results of an ongoing research project on the use of NSM and side-NSM-FRP composites for the purpose of increasing the load-carrying capacity of continuous two-pan RC beams. This research study comprises two parts; an experimental part and a finite element (FE) part. First, three large-scale two-span beams were statically investigated; one control beam and two other beams initially strengthened in bending with two 6 mm diameter CFRP bars. Second, a three dimensional (3D) FE model was developed, using the computer software ABAQUS, in order to predict the flexural performance of the tested beams and to investigate the influence of the models applied to the CFRP-resin-concrete interfaces. The results obtained indicated that the side-NSM-CFRP bars system is a convenient alternative to the conventional one for strengthening continuous beams. For some strengthening configurations, the side-NSM technique proved to be more efficient than the NSM technique, particularly when the CFRP bars were applied solely in the hogging region or the sagging regions. The moment redistribution of strengthened beams was negatively affected when the steel reinforcement ratio in the hogging region was increased. Nevertheless, the moment redistribution degree was significantly affected by the position and arrangement of the CFRP bars. The 3D-FE analysis developed with the cohesive zone model can capture the main aspects observed from the experiments.

Keywords: NSM; Side-NSM; strengthening; continuous RC beam; FEA.

1. Introduction

Strengthening or retrofitting of reinforced concrete (RC) structures is required due to material deterioration, upgrading initial designs or restoring the lost strength of structural members as a result of accidents or natural hazards such as earthquakes. The near surface mounted (NSM) is presently one of the most promising techniques used for strengthening and repairing RC beams. By this technology, the fiber reinforced polymers (FRPs), in different forms (rods, strips, laminate, etc.) could be embedded with an adhesive-epoxy resin or mortar into pre-sawn grooves in the bottom/top concrete covers of the beam

The NSM-FRP technique has proven its advantages in improving the flexural strength of RC beams as compared to the traditional externally bonding technique (EB-FRP) [1-3]. Comprehensive research studies have been conducted for the purpose of experimentally and numerically investigating the behavior of simply supported RC beams strengthened or repaired with NSM-FRP bars [4-8]. The results of the experimental investigations indicated

that the effectiveness of applying the NSM-FRP bars depends on several factors such as continuity, bonding length and characteristics of the FRP reinforcements along with the mechanical properties of the filling material. On the other hand, the numerical investigations revealed that predicting the flexural performance of beams strengthened with NSM-FRP composites, using computer programs based on the finite element (FE) analysis, relies on the constitutive model used to simulate the bond relationship between the FRP and filling material, as well as between the filling material and concrete. In other words, the proper simulation of the interaction between the strengthening system and concrete is essential for creating reliable finite element models (FEMs) for such strengthened structural members. To this end, the available approaches reported in literature can be classified into two main categories: (1) Perfect bond between the CFRP bars and concrete/filling material. This approach ignores the development of shear stresses in the interface materials, and the slip between the reinforcement elements. Almassri et al. [9] found out that by fully embedded the CFRP bars into concrete; the nonconventional failure mode of NSM beams, in particular the concrete cover separation, could be simulated. Sharaky et al. [10] on the other hand, indicated that the perfect bond between concrete and resin could give accurate FE results, compared to the experimental ones, for the beams that experimentally failed at the concrete-epoxy interface or at composite-epoxy interface, while less precise FE results were recorded for the beams failed due to concrete cover separation. (2) The interface contact; this approach is widely used in the literature [10-14] in order to simulate the probability of debonding between CFRP and concrete in the FE analysis. Shomali et al [14] found out that modeling the cohesive layer for the CFRP-concrete interface provides a good estimation of load-deflection behavior compared with the experimental results. However, in this formulation, the interaction behavior between CFRP and concrete can be simulated using a single bond-slip law to represent the overall response of the strengthening components. The bond-slip law is defined by three main parameters: (i) stiffness (k); (ii) ultimate bond strength (τ_m); and (iii) ultimate slip (s_{m}) at debonding.

However, as reported in previous study carried out by the authors on simply supported beams [15], the NSM system might be not feasible or even impossible to set up in several practical cases, starting from limitations of the architectural requirements to those related to the dimensions and reinforcement of the beam itself. The same mentioned study showed that inserting the CFRP rods laterally, adjacent to the longitudinal steel bars inside the pre-cut grooves instead of the beam soffit, as so called the side near surface mounted (side-NSM) technique, could be a convenient method for addressing problems linked to the use of the classical NSM strengthening technique. The side-NSM beams exhibited improvement in the flexural capacity up to 59% over than that of the corresponding unstrengthened beam. In addition, the ductility performance of the side-NSM beams was better than that of the NSM beams. This was principally due to the application of the side technique which caused change or delay the nonconventional failure mode of beams such as CFRP bars pull-out. More recent, the side-NSM technique for strengthening medium-scale simply supported beams was investigated by Haddad et al [16]. The experimental results of their study confirmed efficiency of the side-NSM technique in improving the overall mechanical performances of RC beams, in particular for beams strengthened with CFRP strips at variable profiles (trapezoidal and parabolic profile).

In addition to the limitations of using the NSM technique for strengthening simply supported beams, the need for changing the strengthening position is essential for the continuous RC beams. This is because the continuous RC beams are commonly used in parking garages, overpasses and bridges. In such cases, the side surfaces of the beam are more accessible than the top or bottom surfaces; therefore, using the side-NSM technique for strengthening these types of structures is more feasible. However, in other cases, particularly in ordinary RC buildings, application of the top NSM-CFRP reinforcements in the continuous connection cannot be easily performed due to the presence and continuity of the columns, while applying the CFRP reinforcements laterally, in the top part of the beam/connection, might be more rational. Furthermore, the RC beams in residential buildings are usually narrow, which limits the amount of the FRP that can be provided; hence, the side surfaces can be utilized along with the top or bottom faces to accommodate the appropriate amount of FRPs.

Although most *in-situ* RC beams are statically indeterminate constructions, the application of NSM/side-NSM techniques for strengthening indeterminate RC structures has hardly been studied, and the published design guidelines provide limited provisions regarding the NSM-FRP continuous beams. To date, the behavior benefits, failure mechanism and rate of strength gain of using the NSM/side-NSM CFRP bars strengthening techniques in continuous beams have scarcely been explored and still remain vague concepts to most researchers and practicing engineers. A very recent study [17] showed that, in addition to the above mentioned factors identified for strengthening simply supported beam, the effectiveness of using the NSM technique in continuous RC beam depends on the anchorage length of CFRP bars beyond the inflection point IP (zero moment point). As stated in [17], terminating the CFRP bars before the IP caused a change in the failure mode from debonding to premature detachment of the concrete cover, which caused a 12% decrease in the load-carrying capacity and a 46% drop in the beam ductility as compared to those observed in a beam employed sufficient strengthening length. Furthermore, a significant reduction in the ability of the beam to redistribute moment at failure was observed. To the best of the authors' knowledge, there are no studies in the literature that have been performed for investigating the flexural behavior and failure mode of continuous RC beam strengthened with the side-NSM-CFRP bars.

The present paper concerns with the global performance of RC beams continuous over two spans of 2850 mm each, and strengthened in bending with CFRP bars by using the NSM and the side-NSM technique. In the initial sections of this paper, three full-scale of two-span beams were statically tested: one control beam and two others strengthened beams. Several comparative studies were conducted between the tested beams in terms of failure mode and location, flexural capacity, ductility state and moment redistribution level. Then a three-dimensional (3-D) finite element model for each tested beam was created using the ABAQUS software [18]. Three combinations of bond model and behavior of CFRP bars were investigated; namely: (i) the perfect bond with full tensile strength of the CFRP ($\sigma_{FRP}^{max} = \sigma_{FRP}^{ult}$); (ii) the modified perfect bond with a reduction in the tensile strength of the CFRP ($\sigma_{FRP}^{max} = \alpha\sigma_{FRP}^{ult}$), where $\alpha < 1$; and (iii) the cohesive zone bond model. These models were initially used for exploring impacts of the different interfacial models on the prediction of the ultimate capacity of strengthened NSM and side-NSM beams. For comparison and validation purposes, the results of the FE beams were compared with the experimental results.

Accordingly, the cohesive zone model was adopted for assessing effects of the reinforcement ratio and arrangement, as selected parameters, on the flexural capacity and moment redistribution degree of continuous beams strengthened internally according to the NSM/side-NSM CFRP bars techniques.

2. Experimental work

2.1 Experimental program

For the experimental investigation, three rectangular two-span RC beams were fabricated and tested. One beam was considered as a control beam, and the two others were initially strengthened with Ø6 CFRP bars. The beams were built at the same time with the same size, concrete and steel. The total length, span length, width and depth of each beam were 6000 mm, 2850 mm, 150 mm and 250 mm, respectively. The tested beam specimens were reinforced with the same reinforcement amount composed of two steel bars of 14 mm diameter in flexural and closed stirrups of 8 mm bar diameter in shear. The shear stirrups were uniformly spaced, at equal intervals of 100 mm, along the beam length, as illustrated in Fig.1. The clear concrete cover of the tested beams was maintained at a depth of 25 mm on all sides.

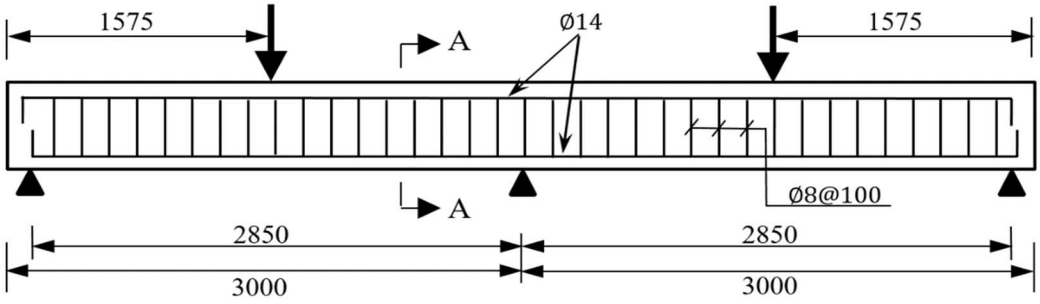

(a) Eleveation view

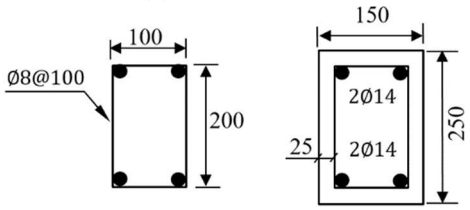

(b) Section A-A

Fig. 1: Dimensions, steel layout as well as support and load arrangement of tested beams. (All dimensions are in mm)

Table 1 provides the designations and details of the control and strengthened beams. Note that beam CB-E was not reinforced with CFRP bars; it was tested for comparison purposes, while beams BC1-E-NSM and BC2-E-SNSM were strengthened with CFRP rods in the hogging and sagging regions. The only difference between the above strengthened beams was the position of the CFRP bars. The NSM technique was used for strengthening beam BC1-E-NSM and the side-NSM technique was used for strengthening beam BC2-E-SNSM. The CFRP bars in the hogging region of each beam were placed symmetrically about the central support; however, the CFRP bars in the sagging regions started from the face of the support without any anchorage over the external supports, as is clearly indicated in Fig.2. In order to avoid the premature peeling off failure mode of beam, the strengthening length to the beam length ratio (SL/BL) was considered equal to 0.7 and 0.65 in the hogging and sagging regions,

respectively, where SL is the distance between the end of the CFRP and the applied load and BL is the distance between the support and the applied load [6,15,19]. In addition, the area of CFRP reinforcement (A_f) to the area of the tension steel reinforcement (A_s) was selected equal to 18% [17] in both hogging and sagging regions. Therefore, the axial stiffness ratio [10] ($1+\frac{E_f \times A_f}{E_s \times A_s}$) of tested beams was approximately 1.16, where E_f and E_s are the Young's modulus of CFRP and steel, respectively. The letter (E) assigned to the beam's name is used to refer to the experimental testing of the beam.

The groove preparation applied procedure is described elsewhere [17]. Grooves measuring 15 mm in both width and depth were made, these dimensions are in accordance with recommendation of the ACI 440.2R guideline [19], i.e. greater than $1.5d_{CFRP}$, in order to avoid premature collapse of the strengthening system. In beam BC1-E-NSM the clear distance between grooves was maintained at 55 mm, which is larger than twice the depth of the groove (30 mm).A surface sand coating was applied to modify the surface state of the initially smooth CFRP rods, as recommended by [20].

Table 1. Test matrix and details of the control and strengthened beams

Beam	FRP Type	Hogging region strengthening			Sagging region strengthening			A_f/A_s (3)	Filling Material	Strengthening technique
		No.	Length(1)	SL/BL(2)	No.	Length(1)	SL/BL			
CB-E	----	----	----	----	----	----	----	----	----	----
BC1-E-NSM	CFRP	2Ø6	2.0	0.70	2Ø6	2.3	0.65	18	Resin	NSM
BC2-E-SNSM	CFRP	2Ø6	2.0	0.70	2Ø6	2.3	0.65	18	Resin	Side-NSM

(1) Length in m; (2) SL: is the distance between end of the FRP bars and the external point load. BL: is the distance between the center support and the external point load; (3) Ratio (%) of the FRP reinforcement (A_f) to the tension steel reinforcement (A_s).

The characteristics of the steel reinforcement and concrete, which were utilized in the formulation of the tested beams, were determined experimentally. Three representative specimens of steel were tested in tension; the average yield strength and Young's modulus obtained were 572.6MPa and 192.5GPa, respectively. Eight specimens of hardened concrete cylinders, with dimensions of 160 mm in diameter and 320 mm in height, were tested in compression/tension at 28 days; the average compressive strength, tensile strength and elastic modulus obtained were equal to 39MPa, 3MPa and 29.2GPa, respectively. As indicated by the manufacturer, the tensile strength and modulus of elasticity of CFRP bars were 2800MPa and 165GPa, respectively.

The beams were tested to destruction under two concentrated loads distanced 2850 mm; one load (P) was placed at middle of each span. Two hydraulic actuators were used to load the beams with a load capacity of 400 kN and an average loading speed 0.3 kN/s each. However, in order to measure the reaction at any level of the applied load, a 200 kN load cell was used as an intermediate support. Two vertical linear variable differential transducer (LVDTs) were used for each beam to monitor the vertical mid-span deflections, as presented in Fig.3. In addition, eight strain gauges, each with a base length of 13 mm, were installed on the CFRP bars, at different positions in order to measure the variation in the longitudinal tensile strain of the strengthening bars.

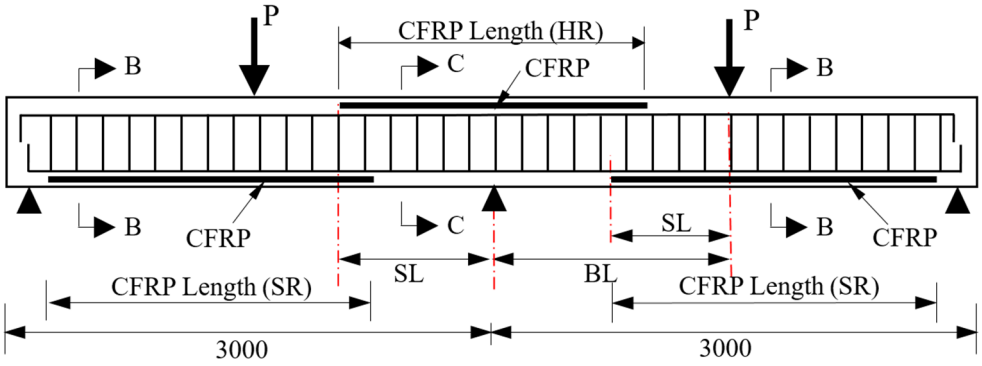

(a) Elevation view of the beam specimens and arrangement of the CFRP bars

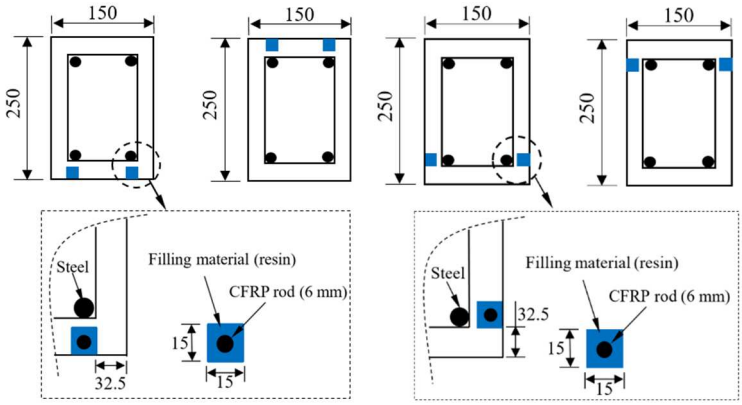

(b) Cross section (B-B & C-C) in beam BC1-E-NSM

(c) Cross section (B-B & C-C) in beam BC2-E-SNSM

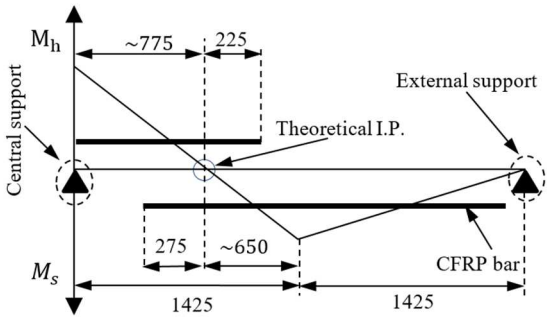

(d) Layout of CFRP bars in strengthened beams

Fig. 2 Beam specimens strengthened with CFRP rods. (All dimensions are in mm)

Fig.3: Test setup and the instrumentations used for testing beams.

2.2 Main test results and discussion

Table 2 provides a summary of the main experimental results of the tested beams in terms of load-carrying capacity (P_u), attained central reaction at the ultimate load level (R_c), ultimate bending moment in the hogging (M_h^{Exp}) and sagging (M_s^{Exp}) regions, moment redistribution ratio (β), ductility index (μ) and energy absorption capacity (E_{ab}). The ductility index (μ) is defined as the ratio of the deflection at ultimate load to the deflection at which the steel starts yielding. The energy absorption capacity E_{ab} is calculated based on the area under the load-deflection curve (Fig.4). This section also presents and discusses the experimental results regarding the longitudinal strain, effectiveness and bond strength of the CFRP bars.

2.2.1 Load deflection response

Fig. 4 displays the relationship between the total applied load and the average deflection at the midspan points of the CB, BC1-E-NSM and BC2-E-SNSM specimens. It is clearly indicated from Fig.4 that the two strengthened beams exhibited a higher load-carrying capacity than that of the unstrengthened control beam, although the side-NSM system turned out to be slightly less efficient than the NSM system in enhancing the flexural strength capacity of RC beam. The beam BC1-E-NSM failed at a load of 277.1kN, which represents a 63.3% increase over the ultimate load of the control beam, CB-E (169.7kN), while the beam BC2-E-SNSM failed at a load of 250.1kN which corresponds to a 47.4% increase over than that of the control beam.

The reason behind the 9.7% reduction in the load-carrying capacity of beam BC2-E-SNSM with respect to that of beam BC1-E-NSM is attributed to the position of the CFRP bars. In the side beam, the CFRP bars were closer to the neutral axis, which led to decrease the effective depth of the tension reinforcements (CFRP and steel). As a result of that, the effective moment arm of the tensile reinforcements decreased within the beam cross section. It is worth mentioning that the reported percentage drop of the ultimate load for the continuous beam specimens tested in the current study is approximately similar to that previously reported for simply supported beams. As stated in [15], inserting the CFRP bars in the vertical sides of the beam instead of the bottom side decreases the load-carrying capacity by about 12.9%.

Compared with the conventional NSM system, Fig.4 also indicates that placing the additional CFRP reinforcement alongside the tension steel bars proved to increase the average midspan deflection of the strengthened beam, thereby improving the displacement ductility index (μ) and energy absorption capacity (E_{ab}) (see Table 2). Among all the tested beams, beam BC2-E-SNSM exhibited the highest deflection ($\delta_u = 58.9$ mm) at the ultimate load level (P_u), while beam BC1-NSM presented the lowest value ($\delta_u = 50.58$ mm). The midspan deflection of beam BC2-E-SNSM at the end of the test (δ_f) was 63.9 mm, whereas it was 50.6 mm for beam BC1-E-NSM. These two results of deflection are about 27.1% and 42.2% lower than the deflection at the midspan of the control beam (δ_f =87.6mm), respectively.

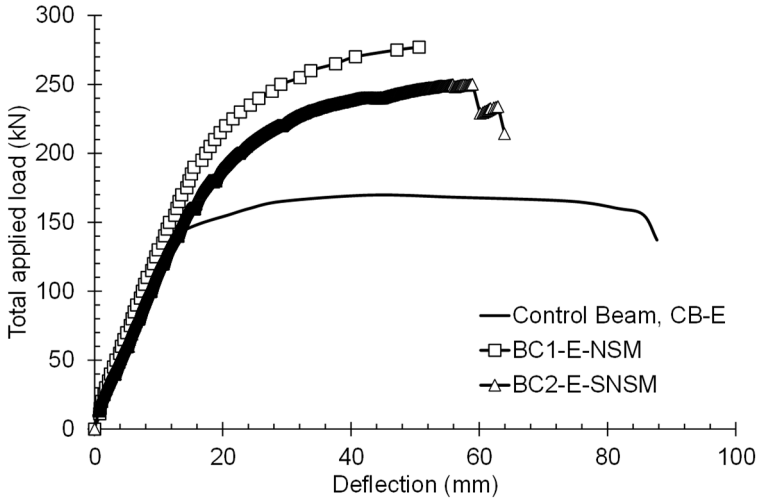

Fig.4: Load deflection curve of tested beams

Table2. Main experimental results of control, NSM and SNSM beam.

Beam	Ultimate load (P_u)	Central support reaction[1] R_c	Flexural moment at hogging (M_h)			Flexural moment at sagging (M_s)			μ[7]	E_{ab}[8]
			M_h^{Exp}[2]	M_h^{Th}[3]	$\beta(\%)$[6]	M_s^{Exp}[4]	M_s^{Th}[5]	$\beta(\%)$[6]		
CB-E	169.7	110.1	36	45.3	20.53	42.5	37.8	-12.43	4.8	8082.8
BC1-E-NSM	277.1	180.3	59.5	74	19.59	69	61.7	-11.83	3.3	10356.6
BC2-E-SNSM	250.1	166.6	59.3	67	11.49	59.4	55.6	-6.92	3.6	11242.1

(1) Central reaction measured by attached load cell at ultimate load P_u. (Both in kN); (2) Experimental ultimate negative moment calculated by: : $M_h^{Exp} = \frac{(P_u - 2R_c)\times L}{4}$, where L is the beam length. (kN.m); (3) Theoretical ultimate negative moment calculated by: $M_h^{Th} = \frac{3P_u L}{32}$. (kN.m); (4) Experimental ultimate positive moment calculated by: $M_s^{Exp} = \frac{(P_u - R_c)\times L}{4}$. (kN.m); (5) Theoretical ultimate positive moment calculated by: $M_s^{Th} = \frac{5P_u L}{64}$. (kN.m); (6) Moment redistribution calculated by: $\beta\,(\%) = \left(\frac{M^{Th} - M^{Exp}}{M^{Th}}\right) \times 100\%$. ; (7) Ductility index.; (8) Energy absorption capacity. (KN.mm).

2.2.2 Failure mode and cracks pattern

Fig. 5 shows the classical flexural failure of control beam specimen; concrete crushing after yielding of tension steel.

The typical failure mode of beams strengthened with NSM/side-NSM CFRP bars was due to the yielding of the tension steel reinforcement followed by debonding of the strengthening components. The debonding failure of beam BC1-E-NSM was brittle as a consequence of the sudden pulling-out of the CFRP bars in the hogging region close to the central support, with minor concrete crushing at the applied load points, as illustrated in Fig.6. On the other hand, the debonding failure of beam BC2-E-SNSM was characterized by cracking of the epoxy-resin cover and fracture in the concrete at the hogging and sagging regions, with a high intensity concrete crushing at the applied load points and minor concrete crushing at the central support, as depicted in Fig.7. In beam BC2-E-SNSM, longitudinal cracks appeared after yielding of the tension steel at the resin-concrete interface in the hogging and sagging regions. These cracks gradually merged to the adjacent flexural cracks which had previously formed in the regions close to the points of loading and over the central support. It should be noted that wide flexural cracks emerged in the hogging regions of beams CB-E and BC1-E-NSM before failure. These wide cracks were not observed in the case of beam BC2-E-SNSM.

A small hammer along with chisel were cautiously used to check the constancy of the embedded CFRP bars in the hogging regions of beams BC1-E-NSM and BC2-E-SNSM. It was found that, in each beam, one extremity of the CFRP bars moved from its initial position towards the central support, indicating that debonding failure occurred at the resin-CFRP interface. This displacement of CFRP bars was more conspicuous in beam BC1-E-NSM than in beam BC2-E-SNSM.

Interestingly, it was noticed that in the strengthened beams, the flexure cracks extended beyond the inflection points, i.e. zero moment points, as a result of applying the CFRP bars (Figs. 6-7). Compared to the control beam, the number of the cracks in beam BC1-E-NSM was higher by 200% and 62.5% in the hogging and sagging region, respectively; whereas the number of the cracks in beam BC2-E-SNSM was higher by 250% in the hogging region and 193.8% in the sagging region.

Table 3 presents the flexural crack width values in the hogging region over the central support of tested beam specimens. The crack width was measured up to the beam's yielding load point by using a special microscope with an accuracy of 0.05 mm. Table 3 demonstrates

that the position of the additional reinforcement has limited impact on the development of the crack width. The measured crack width in beam BC2-E-SNSM was turned out to be slightly larger than that in beam BC1-E-NSM for the same applied load.

2.2.3 Experimental bending moments and moment redistribution

The total applied load versus the bending moments of tested beams CB-E, BC1-E-NSM and BC2-E-SNSM at the critical sections (sagging and hogging regions) are presented in Fig.8a. The mid-span bending moment (sagging moment) is shown with a positive sign and the intermediate bending moment (hogging moment) is shown with a negative sign. In order to assess the amount of moment redistribution, the elastic bending moment was computed by considering a uniform flexural stiffness throughout the entire length of the beam. Moreover, the experimental bending moment at any level of the applied load was calculated based on equilibrium considerations of the beam using the measured central support reaction (Fig.8b). As can be observed in Fig.8b, the experimental central support reaction, in beams CB-E and BC1-E-NSM, suddenly shifted from the elastic reaction once the tension steel yielding load was reached. This involved more loads transferred to the external supports, leaving the central support with less load. The sudden shift could mainly be accredited to the wide cracks that appeared over or close to the middle support, which changed the reaction system of continuously supported beams (see section 2.2.2).

(a) Central support (b) Left span (c) Right span

Note: (1)Number of the cracks in the hogging region: 8; (2)Number of the cracks in the sagging religion (maximum number): 16

Fig.5: Failure mode of control beam, CB-E

(a) Central support (b) Left span (c) Right span

Note: (1)Number of the cracks in the hogging region: 24; (2)Number of the cracks in the sagging religion (maximum number): 26

Fig.6: Failure mode of beam BC1-E-NSM

(a) Central support (b) Left span (c) Right span

Note: (1)Number of the cracks in the hogging region: 28; (2)Number of the cracks in the sagging religion (maximum number): 47

Fig.7: Failure mode of beam BC2-E-SNSM

However as can be seen in Fig.8a, the elastic model cannot accurately reflect the evolution of the actual bending moment. The actual bending moment of the beams at a low load level showed approximately a linear development, while the load increased, the development of the actual bending moment differed from the elastic one and it showed a nonlinear behavior. At the ultimate load, the experimental negative and positive moments of the tested beams were, respectively, lower and larger than the elastic moments, indicating moment transfer occurred from the inner support towards the midspan. In general, among the tested beams, the values of the experimental bending moment of the side-NSM beam (i.e. BC2-E-SNSM) were the closest to the values of the elastic bending moment. For example, the experimental hogging moment at the failure load, calculated from the measured central support reaction of beams CB-E, BC1-E-NSM and BC2-E-SNSM, were 36kN.m, 59.5kN.m and 59.3kN.m, respectively. These results represent 79.47%, 80.41% and 88.51% of the calculated elastic moment of 45.3kN.m (for CB-E), 74kN.m (for BC1-E-NSM) and 67kN.m (for BC2-E-SNSM).

Table 3. Crack width of tested beams at different load levels.

CB-E		BC1-E-NSM		BC2-E-SNSM	
P_t (kN)	w_{cr} (mm)	P_t (kN)	w_{cr} (mm)	P_t (kN)	w_{cr} (mm)
30	0.2	30	0.08	30	0.15
50	0.35	50	0.1	50	0.21
70	0.53	70	0.15	70	0.26
90	0.62	90	0.25	90	0.3
110	0.75	110	0.33	110	0.43
130	1.35	130	0.42	130	0.55
150	3.1	150	0.53	150	0.61
-----	-----	170	0.62	170	0.76

The moment redistribution could refer to the ability of an indeterminate RC structure to form a sufficient number of hinges under increasing the applied load. These hinges usually allow transferring the moment in accordance with their formation and position. In this study, the capacity of the tested beams to redistribute moment was assessed and concluded in Table 2. The control beam and the beam strengthened with NSM-CFRP bars exhibited almost similar trends to redistribute moment. They failed, however, at different loads. On the other hand, in accordance with the reinforcement ratio adopted in this experimental program, it was found that placing the CFRP bars laterally, adjacent to the steel reinforcement using the side-NSM technique, decreases the moment redistribution capacity of the beam. The moment

redistribution ratio (β) of the control beam was 20.5% at central support and -12.4% at midspan; however, beams BC1-E-NSM and BC2-E-SNSM had respectively moment redistribution of 19.6% and 11.5% at the central support, and -11.8% and -6.9% at mid-span.

2.2.4 Longitudinal strain and effectiveness of the CFRP bars

Figs. 9a and 9b show the variation in the longitudinal tensile strain of the CFRP bars for beams BC1-NSM and BC2-SNSM respectively, at different load levels. The strains are presented for half of the beam length, i.e. from the exterior support of the right span to the interior support. Owing to the configuration of the CFRP bars in beam BC1-E-NSM, it was expected that the CFRP bars in the critical sections would demonstrate a high strain response at the ultimate load level in comparison with the CFRP bars in beam BC2-E-SNSM. Such anticipation has not been exhibited by beam BC1-E-NSM, as can be discerned from Fig. 9. Although the two strengthened beams failed at different loads, the maximum measured tensile strain of CFRP bars over the central support, in beams BC1-E-NSM and BC2-E-SNSM, were found equal to 0.0126 mm/mm and 0.0123 mm/mm, respectively. This can be justified by the fact that the failure of the two strengthened beams was primarily due to the collapse of the strengthening systems (i.e. debonding failure). However, regarding the remaining strain-gauges attached to the longitudinal direction of CFRP bars, the measured CFRP strains (Fig.9) in beam BC1-E-NSM at the ultimate load level exhibited a relative increase in comparison with the CFRP strain measured in beam BC2-E-SNSM for the same position of the gauge. The main observation pertained to the strain value at the elastic inflection point, i.e. at a length of 2070 mm from the external support. At the ultimate load level, the increase in the tensile strain of CFRP bars at that point was evident in beam BC1-E-NSM compared to that reported in beam BC2-E-SNSM. This increasing in the ultimate strain could be imputed to the amount of moment redistribution as well as to the wide cracks that formed before the beam's failure; these cracks changed the location of the inflection point in beam BC1-E-NSM to a new position beyond the elastic one.

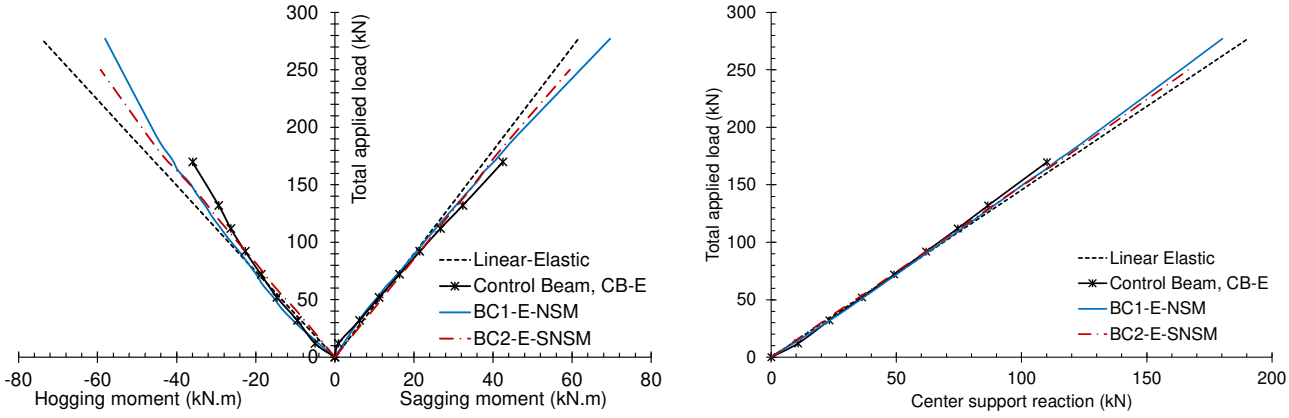

(a) (b)

Fig.8: Total applied load versus (a) bending moment; (b) central support reaction

Effectiveness of the CFRP bars for strengthening continuous RC beams was evaluated in beams BC1-E-NSM and BC2-E-SNSM on the basis of the utilization level ($\frac{\varepsilon_{CFRP}}{\varepsilon^{ult}_{CFRP}}$) at the critical sections, as reported in Table 4. As can be noticed from Table 4, none of the specimens

reached the ultimate CFRP rupture strain (0.017 mm/mm) and the reported debonding strain was marginally affected by the position of CFRP reinforcement. The $(\frac{\varepsilon_{CFRP}}{\varepsilon_{CFRP}^{ult}})$ of NSM-CFRP bars at the ultimate load was 74.3% at central support and 68.9% at midspan section. On the other hand, the $(\frac{\varepsilon_{CFRP}}{\varepsilon_{CFRP}^{ult}})$ of side-NSM-CFRP bars at the ultimate load was about 72.2% at central support and 69.8% at midspan section.

2.2.5 Bond analysis of the CFRP bars

In general, the bond strength of NSM-FRP bars ranges from 3.5MPa to 20.7MPa [21-22], which is influenced by many factors such as the groove size, section type, surface state and development length of the CFRP bars as well as by the mechanical properties of the filling material. The ACI 440.2R guideline [19], for instance, recommends the average bond strength as 6.9MPa for calculating the development length of the NSM-FRP bars. However, in the present paper, the experimental average bond stress (τ), between two consecutive strain gauges, was calculated according to Eqs. (1) and (2) by taking into account the measured experimental strain (see Fig.9), where i refers to number of the strain gauge and σ, ε, E_{CFRP}, l, d_{CFRP}, A_{CFRP} are, respectively, the tensile stress, strain, modulus of elasticity, length, diameter, and area of the CFRP bars.

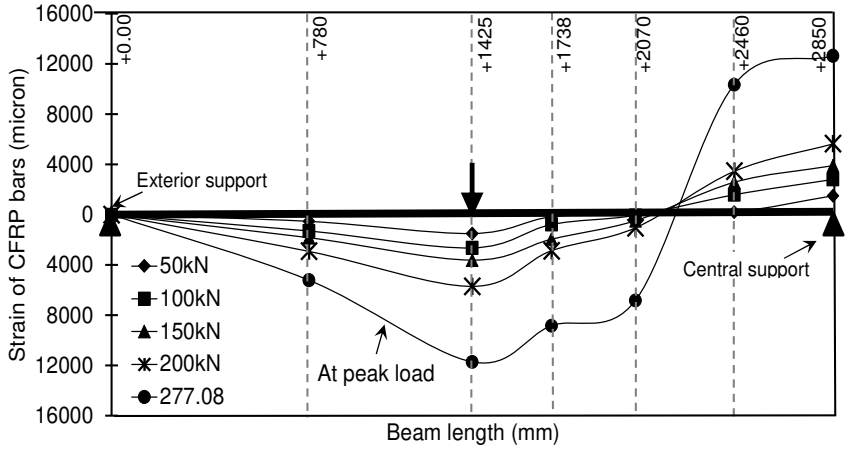

(a) BC1-E-NSM

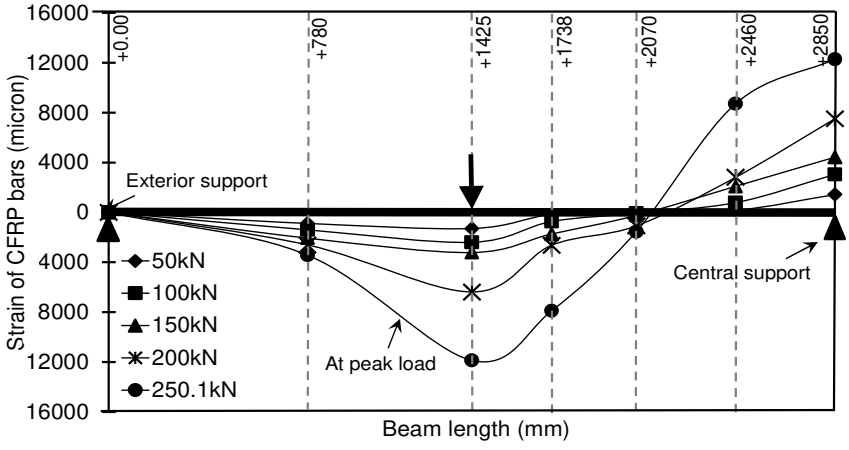

(b) BC2-E-SNSM

Fig.9: Variation in longitudinal strain of FRP bars at different loads.

Table 4. Tensile strains of CFRP bars at different load levels.

Load (kN)	BC1-E-NSM				BC2-E-SNSM			
	Central support		Mid-span		Central support		Mid-span	
	ε_{CFRP} (Micron)	$\frac{\varepsilon_{CFRP}}{\varepsilon_{CFRP}^{ult}}$	ε_{CFRP} (Micron)	$\frac{\varepsilon_{CFRP}}{\varepsilon_{CFRP}^{ult}}$	ε_{CFRP} (Micron)	$\frac{\varepsilon_{CFRP}}{\varepsilon_{CFRP}^{ult}}$	ε_{CFRP} (Micron)	$\frac{\varepsilon_{CFRP}}{\varepsilon_{CFRP}^{ult}}$
50	1500	0.088	1497.5	0.088	1493	0.088	1290	0.076
100	2812	0.165	2640	0.155	3039	0.179	2393	0.141
150	3907	0.230	3628	0.213	4435	0.261	3207	0.189
200	5647	0.332	5707	0.336	7510	0.442	6389	0.376
250.1	9948	0.585	9399	0.553	12278	0.722	11862	0.698
277.1	12639	0.743	11717.5	0.689	----	----	----	----

$$\sigma_{((i+1)-i)} \times A_{CFRP} = \tau_{((i+1)-i)} \times (l_{(i+1)} - l_i) \times d_{CFRP} \times \pi \quad (1)$$

$$\tau_{((i+1)-i)} = \frac{(\varepsilon_{(i+1)} - \varepsilon_i) \times E_{CFRP} \times d_{CFRP}}{4 \times (l_{(i+1)} - l_i)} \quad (2)$$

Fig. 10 indicates that the bond stress increases with the applied load. The maximum values of τ reported for beams BC1-E-NSM and BC2-E-SNSM were 6.4MPa and 5.6 MPa, respectively. These maximum values were recorded at the same location of the beams' failure, i.e. in the hogging regions between the central support and end of the CFRP composite. The slight decrease in the τ value at the ultimate load for beam BC2-E-SNSM with respect to the τ value for beam BC1-E-NSM could be assigned to the drop in the measured strains resulting from the change of the position of CFRP bars, as discussed in the previous section.

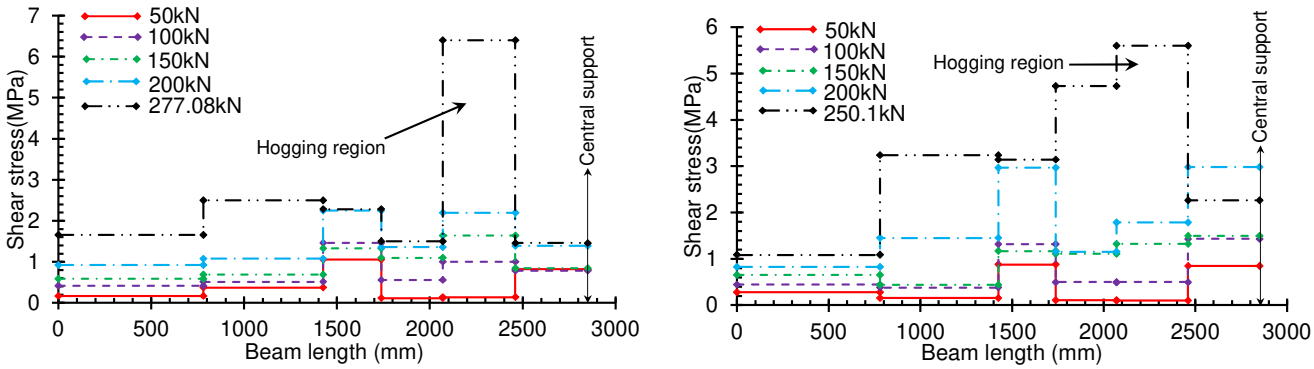

(a) BC1-E-NSM

(b) BC2-E-SNSM

Fig.10: Experimental average shear stress

3. Numerical investigation

The objective of this part is to utilize the FE package ABAQUS version 6.13 [18] for creating an efficient and reliable 3D model that can simulate and predict the behavior of continuous RC beams strengthened internally with CFRP bars. In addition, for investigating the effect of using different models of CFRP/resin-concrete interface on predicting the ultimate strength capacity of strengthened beams.

The ABAQUS-standard software uses a non-linear procedure, which is suitable for FE

analysis and computer-aided engineering. FE failure analysis was performed to model the tested beams; one of the beams was control beam (CB-E) and the other two beams, namely BC1-E-NSM and BC2-E-SNSM, were strengthened with CFRP bars by using the NSM and side-NSM technique, respectively. Dynamic explicit analysis in ABAQUS with the quasi-static approach was employed by applying a very slow loading in order to make the model converges to the static solution. The dynamic analysis is popularly used instead of the static analysis to help solve of the highly non-linear behavior of cohesive contact in ABAQUS. It has also been applied to other problems such as external CFRP strengthening impact [23], cracks and failure of concrete [24] and push out tests simulations [25]. The accuracy and reliability of the results of the FE dynamic analysis approach were checked for each model during the loading process by comparing the total kinetic energy with the total internal energy. As recommended in the ABAQUS manual [26]; the ratio of the kinetic energy to the internal energy must be less than 5%.

Both the geometric and material nonlinearity, according to the experimental tests, were considered in the numerical solutions. The analysis was operated by means of the displacement control method in order to overcome the convergence difficulties as well as the rigid body modes when two bodies are disconnected in contact pairs [27].

The RC beam is composed of four components; they are the concrete, steel reinforcement, CFRP bars and epoxy-resin adhesive. These components were modeled as separate parts; however, the constitutive laws that are described in the following sections allow identifying their interactions.

3.1 Material properties

3.1.1 Concrete

The classical concrete damage plasticity (CDP) available in ABAQUS [18] library was adopted to model the complex nonlinear behavior of concrete in the simulation test of RC beams. This material model, which has widely been used, provided accurate results [28-30]. The CDP offers the best modeling of the real behavior of concrete and other quasi-brittle materials. It is generally, suitable for material with different yield strength in tension and compression. The CDP assumes the flow rule of non-associated plasticity, which is in accordance with the assumption that the plastic potential function and the yield surface do not coincide with each other. The software ABAQUS uses the Drucker-Prager hyperbolic function for the flow potential. The concrete damage plasticity model assumes that the main failure modes of concrete are cracking in tension and crushing in compression.

In relation to the mechanical properties applied for simulating concrete, the experimental results obtained from the compressive and tensile tests of eight concrete cylinder specimens were used, as reported in section 2.1. The compressive stress-strain relationship for concrete (Fig.11a) was constructed based on the strain readings from the attached strain-gauges on the surface of the tested concrete cylinders. On the other hand, for the full behavior of concrete under uniaxial tensile stress, the modified model, developed by Wahalathantri et al. [31], was used, as given in Fig.11b.

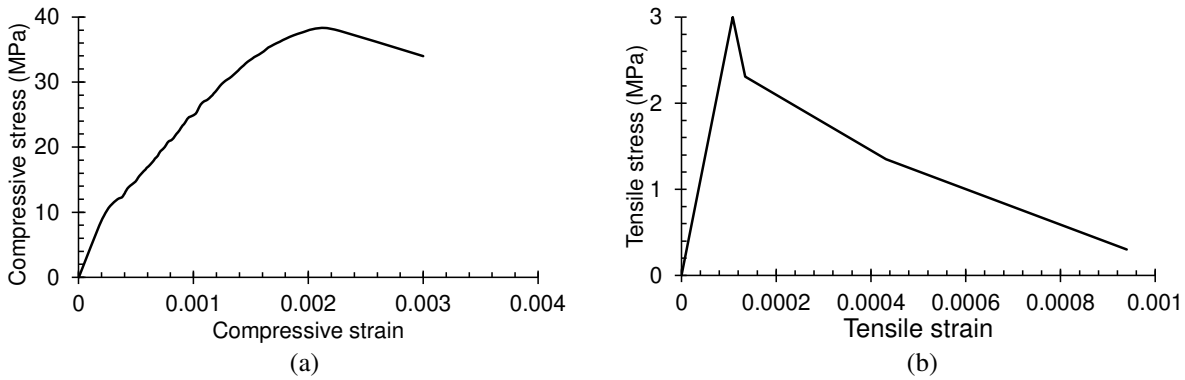

Fig.11: Response of concrete to uniaxial loading in (a) compression and (b) tension

In the concrete damage plasticity, concrete degradation is characterized by two independent variables, namely the degradation of concrete under compression (d_c) and degradation of concrete under tension (d_t). It is important to know that when the damage variable is equal to zero, the concrete is not damaged; whereas when it is equal to one, the concrete is totally damaged [28]. Calculation of the quantities d_c and d_t was performed according to the recommendations of Alfarah et al. [32]; as given by Eqs. (3) and (4), respectively.

The calibration of the CDP model was done according to the recommendations of [10, 26, 33]. The dilatation angle (ψ), flow potential eccentricity (ϵ), stress ratio (σ_{bo}/σ_{co}) and K_c are the main parameters that define respectively the concrete internal friction angle, the rate at which the hyperbolic flow potential approaches its asymptote, the ratio of the biaxial compressive yield stress to the uniaxial compressive yield stress, and the ratio of the second stress invariant on the tensile meridian. The values of the aforementioned parameters were taken as $\psi = 36$, $\epsilon = 0.1$, $\frac{\sigma_{bo}}{\sigma_{co}} = 1.16$ and $K_c = 0.667$.

$$d_c = 1 - \frac{\sigma_c}{\sigma_{c\,ult}} \tag{3}$$

$$d_t = 1 - \frac{\sigma_t}{\sigma_{t\,ult}} \tag{4}$$

3.1.2 Steel and CFRP reinforcement

The elastic modulus, yielding and ultimate strengths of the steel bars were determined experimentally, as previously discussed in section 2.1. The nonlinear tensile stress-strain relationship obtained from the uniaxial tests, on three representative specimens, was assigned to the steel rebar as indicated in Fig.12. The software ABAQUS could then establish the behavior of the multi-axial stress state. A Poisson's ratio of 0.3 was used for the steel reinforcement, and the bond between the steel bars and concrete was assumed to be perfect by using the embedded region contact. This can be justified by the sufficient anchorage length of the steel bars and plenty of friction between the steel and concrete.

According to the manufacturer's instructions, the tensile stress-strain behavior of CFRP reinforcement is linearly elastic up to failure, as shown in Fig.13. The elastic modulus, ultimate strength and Poisson ratio of the CFRP bars used were equal to 165GPa, 2800MPa

and 0.35, respectively.

3.1.2 Epoxy-resin filling material

The stress-strain relationship of the epoxy-resin material was considered as a bi-linear curve in the FE model [27]. The tensile resistance, modulus of elasticity and Poisson ratio of the resin were taken as 29.5MPa, 4.94GPa and 0.37, respectively.

3.2 Interaction and contact conditions

In general, it is important to take into account the interaction between the components of the FE model (concrete, steel, ..etc.) in order to accurately simulate the behavior of the tested beams. The prediction of the flexural performance of RC beams strengthened with FRP composites by using computer programs, based on the FE analysis, is strongly associated with the constitutive model used to simulate the bond behavior between the strengthening components (CFRP bars and resin) and concrete. The bond behavior has an influence on the ultimate strength of the strengthened beam as well as its serviceability aspects such as cracks formation and spacing. In this study, the embedded element option, available in the ABAQUS software, was used to describe the contact between the steel reinforcements and concrete, so one may consider that all degrees of freedom of the nodes of the steel bars and stirrups were subjected to the nodes of concrete. Regarding the interaction between the additional reinforcement/resin and concrete, two different bond models were separately assumed: the perfect bond model (PBM) and the cohesive zone model (CZM). These two models are discussed in the following sections.

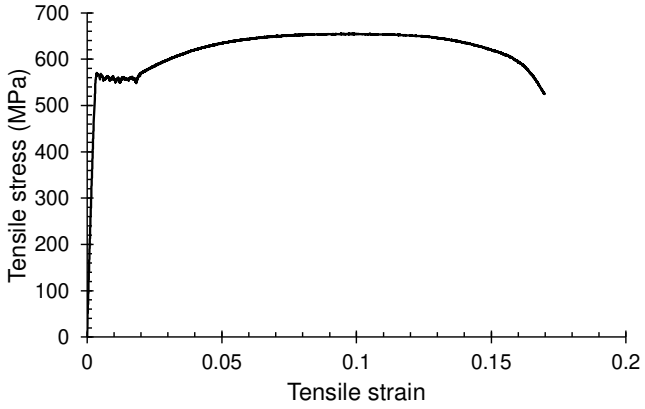

Fig.12: Constitutive model of steel reinforcement

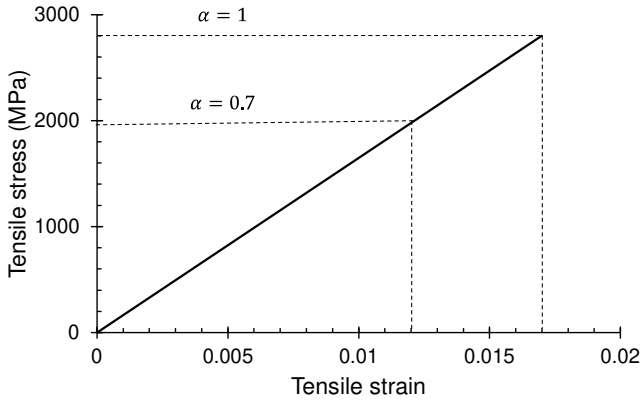

Fig.13: Constitutive model of CFRP reinforcement

3.2.1 Perfect bond model (PBM)

This approach ignores the development of shear stresses in the interface materials and the slip between the reinforcing elements. Furthermore, it does not include fracture of the bond. Researchers usually use this assumption to simplify the modeling behavior [9, 10, 34]. The overall concept of the PBM can be described as follows: (i) The contact between resin and concrete is taken as a perfect bond; and (ii) The CFRP bars are embedded into the epoxy resin

using the embedded contact option, (Fig.14).

In the present study, the PBM was modified by reducing the nominal tensile strength and strain of CFRP by a debonding factor, α ($0.5 < \alpha < 1$) [17] in order to take into account the sliding/fracture that occur between the CFRP/filling material and concrete. Therefore, within the framework of this research, a value of 0.7 was selected for the parameter α according to the utilization level of the CFRP bars (see section 2.2.4). The modified PBM was used to validate the mechanical properties of the materials (CFRP, resin,..etc.) and to verify accuracy of the experimental results.

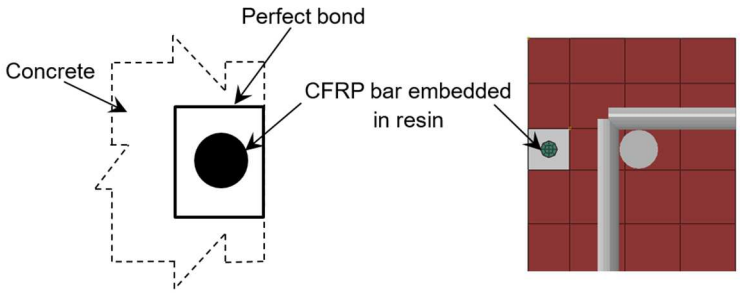

Fig.14: Perfect bond model

3.2.2 Cohesive zone model (CZM)

In this approach, the overall response of the strengthening system (NSM or SNSM) was modelled as a very thin cohesive layer of 1 mm in thickness. The cohesive layer was created by using the offset option available in ABAQUS; and it is located between the CFRP bar and concrete, as depicted in Fig.15. The cohesive layer was tied to the concrete surface, nevertheless, the probability of debonding in the numerical analysis could be obtained by giving the implemented cohesive zone the values of the parameters those define the bond-slip curve. According to [22, 35], there is no data available on the relative slip at the resin-concrete interface. Therefore, the only bond-slip curve used in this research is the one shown in Fig.16 [1], where τ_m is the maximum shear strength, s_m is the ultimate slip, a is a curve-fitting parameter obtained by equating the area underneath the ascending branch of the experimental curve to the value of $(\frac{\tau_m s_m}{1+a})$, and G_{cr} is the fracture energy which is defined as the area under the bond-slip curve.

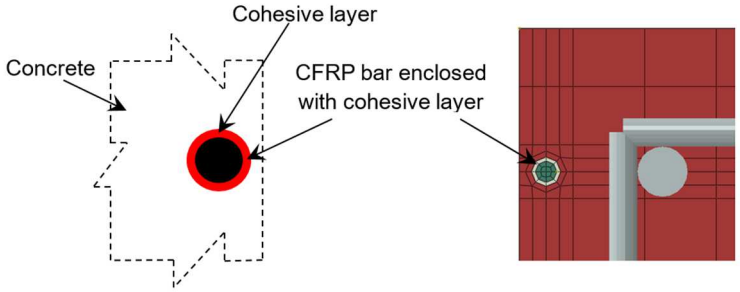

Fig.15: Cohesive zone model

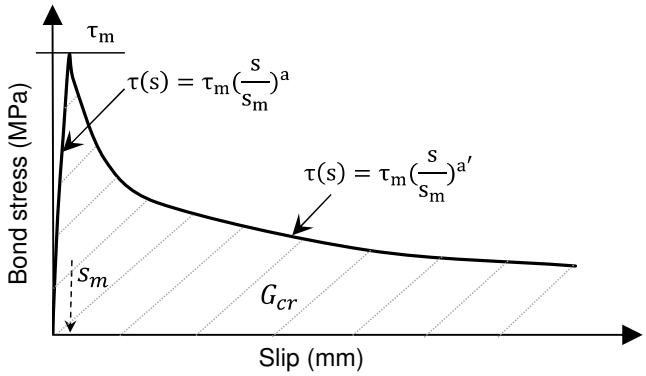

Fig.16: Bond slip law

Several experimental tests were carried out on the basis of the direct pull out test to evaluate the bond stress-slip relationship of the NSM-FRP system [21, 22, 36, 37]. In fact, the results concerning the maximum shear strength have ranged from 3.5 to 20.7MPa. Results from pull out tests on 25×25 mm groove specimens, which were conducted by Al Mahmoud et al. [36], have suggested values for the τ_m, s_m and a parameters; giving τ_{max}= 12.2/0.4, s_m= 0.16/0.05 and $a = 0.74/0.04$. For their part, De Lorenzis et al. [22] carried out a series of experimental pull out tests in order to investigate the effect of several factors, such as the groove size (14mm-24mm), groove-filling material (epoxy/cement) and type of the FRP (CFRP/GFRP) on the bond performance of NSM-FRP bars in concrete. The reported maximum shear strength τ_m for the CFRP bars specimens with epoxy-filled grooves was ranged between 7.24MPa and 16.56MPa, while the measured ultimate slip s_m was ranged between 0.034 mm and 0.372 mm. Furthermore, the experimental pull out tests conducted by Capozucca [37] on 20×20 mm groove specimens showed that the bond strength τ_m value when failure occurred at the epoxy-CFRP rod interface was about 7.2MPa, while the bond strength value when the failure takes place at the epoxy-concrete interface was about 3MPa. Seracino et al. [38] proposed an expression (Eq. 5) to calculate the interface shear stress of NSM-plate-to-concrete joints, while considering the geometry of the debonding based on the statistical analysis of experimental values. Applying Eq. (5), in the present study, gives τ_m=7.9MPa.

$$\tau_{max} = (0.802 + 0.078\varphi)fc^{0.6} \text{ (MPa)} \quad (5)$$

Where φ is the aspect ratio of the interface failure plane calculated from Eq. (6), and fc is the concrete compressive strength.

$$\varphi = \frac{Groove\ depth+1}{Groove\ width+2} \text{ (mm)} \quad (6)$$

However, the numerical simulation showed that the value of τ_m = 12.2 MPa significantly overestimated the ultimate strength of the tested beams, since the CFRP rupture induced the failure instead of the interfacial debonding that was observed in the experiments (Fig.17).

Hence, the τ_m was reduced to 6MPa by taking advantage of the computed bond strength from the experimental study (see section 2.2.5); based on the fact that the bending tests are more adequate to describe and define the actual bond-slip law.

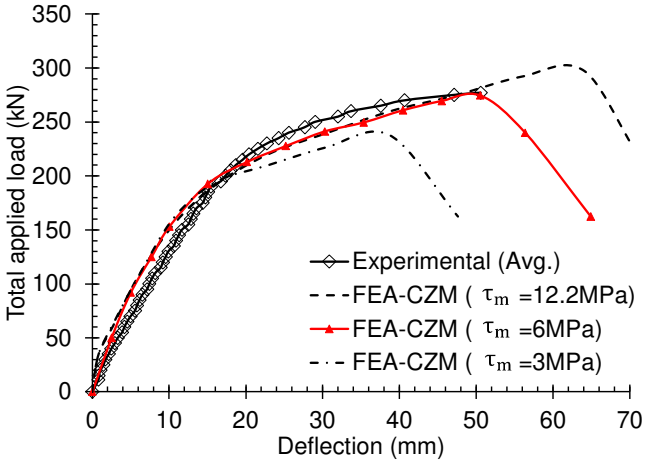

Fig.17: Comparison between the experimental results and FEA results with different value of maximum shear stress for beam BC1-E/N-NSM

The quadratic traction function, which is similar to the cohesive contact approach that is available in literature [39], was adopted to indicate the initial damage of the cohesive layer, as given in Eq. (7), where σ_n is the cohesive normal tensile stress, τ_s and τ_f are the shear stresses of the interface. The characters $n, s, and\ t$ refer to the stress directions. The initial values of the above stresses were taken as σ_n^0: tensile strength of concrete = 3MPa and τ_s^0= τ_t^0= 6MPa. The evolution of the interface damage was expressed in terms of energy release [23], and the value of the calibrated fracture energy G_{cr} used in this FE study was 15mJ/mm2.

$$(\frac{\sigma_n}{\sigma_n^0})^2 + (\frac{\tau_s}{\tau_s^0})^2 + (\frac{\tau_f}{\tau_f^0})^2 = 1 \qquad (7)$$

3.3 Finite element modelling of tested beams

Three combinations of bond models and behavior of CFRP bars were examined and analyzed. These are the perfect bond with the full tensile strength of CFRP ($\sigma_{FRP}^{max} = \sigma_{FRP}^{ult}$), the modified perfect bond with 70% tensile strength of CFRP ($\sigma_{FRP}^{max} = 0.7\sigma_{FRP}^{ult}$), and the cohesive zone bond model.

Fig. 18 shows the boundary conditions, steel skeleton and meshing of the beam model. By taking advantage of the double symmetry of the beam specimen, a symmetry simplification was introduced, as shown in Fig.18a. Only a quarter of the beam, involving two CFRP rods (one rod in the hogging region and the other rod in the sagging region), was modeled (Fig.18b). This helped to make the numerical modeling easier and to reduce the computational time as well. To guarantee the stability of the model, symmetric boundary conditions were applied to the surfaces of the symmetric plans. All the nodes of surface 1, as shown in Fig. 18b, were prevented from moving along the X axis and from turning about the Y and Z axes (Ux = Ry = Rz = 0); while for the nodes of surface 2, the translational displacement along the

Z axis as well as the rotational displacement about the X and Y axes were restrained (Uz = Rx = Ry = 0).

Convergence of the numerical solution was checked through the use of coarse (50 mm) and fine mesh (20 mm) sizes. The numerical load-deflection curves of beam BC1-E-NSM was compared with the experimental one, as shown in Fig.19. As can be seen from Fig.19 the difference between the FE load-deflection curves is not large. This is because the interface region between the CFRP bars and concrete, in the both referred mesh trials, was also refined with a mesh size of 3 mm in order to achieve accurate results (see Fig.15). However, the mesh size of 20 mm was selected as an overall size for the all specimen models throughout this paper, while reducing the mesh size in the region around the CFRP bars to 3 mm. To mesh the components of the beam, different types of mesh elements available in the ABAQUS library were used. Concrete, resin and CFRP bars were meshed with an eight-node 3D hexahedral brick element with reduced integration stiffness, (C3D8R). The steel bars and stirrups were meshed with a two-node 3D truss element type (T3D2). The cohesive layer was meshed with an eight-node 3D cohesive element (COH3D8).

In this FE analysis study, the loading was downward implemented displacement applied on the top surface of the beam, at the mid-span, as a distributed load over a surface similar to that of the loading plate that was employed in the experiments ($100 \times 150mm$). This load was defined as an imposed displacement and applied as a loading rate by using the smooth amplitude function in order to reduce the dynamic analysis time.

Henceforth, for organizational purposes, the letter (E) which was assigned to the beam's name in the experimental sections has been replaced with the letter (N) in the following sections in order to indicate that the beam is numerically investigated.

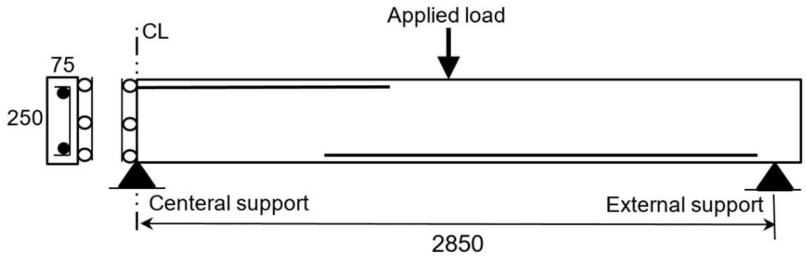

(a) Symmetry simplification (Dimensions in mm)

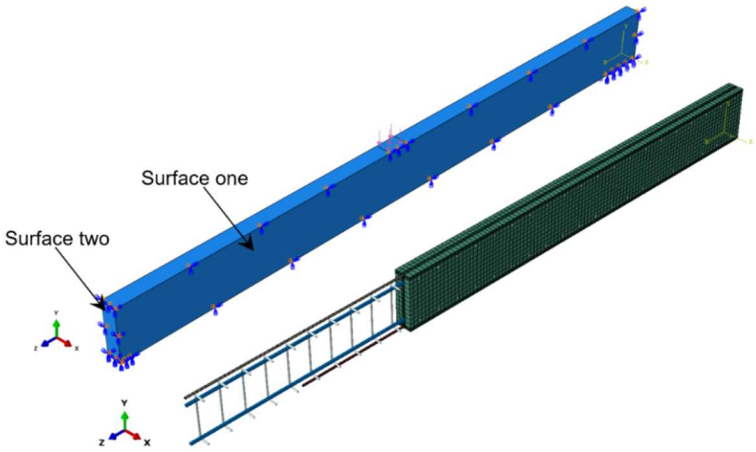

(b) Boundary conditions, steel Skelton and finite element mesh of quarter beam

Fig.18: Detail and boundary condition of the FE beam (all dimension are in mm)

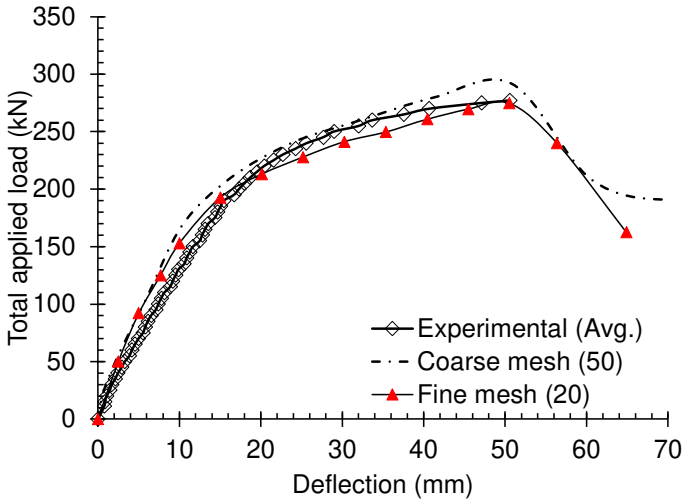

Fig.19: Effect of the mesh size

3.4 Finite element results and discussion

3.4.1 Load deflection response

Fig. 20 shows the load-deflection ($P-\delta$) curves for the control and strengthened beams (CB-E, BC1-E-NSM and BC2-E-SNSM) obtained from the experiments and the finite element (FE) analysis. In general, there is a good correlation between the numerical and experimental results in terms of the ultimate load and deflection. As expected, the largest difference between the numerical and experimental results was reported when the conventional PBM ($\alpha = 1$) was employed, whereas there is a quite satisfactory convergence was observed when using the modified PBM ($\alpha = 0.7$) and the CZM.

For the control beam, Fig.20 a, the excellent agreement between the experimental and the FE analysis results is clear. The stiffness and flexural load capacities of the beam were well predicted by the numerical model. The little difference between stiffness of the experimental curve and that of the FE curve is probably attributed to: (i) The perfect bond assumed between concrete and steel reinforcement, and (ii) the presented average deflection; i.e here, at any level of the applied load the experimental deflection of the beam was computed as the average value of the left and right span deflections.

Regarding the strengthened beams (Figs.20b and 20c), the results obtained from the FE analysis, using the different bond models, were identical to the experimental results found before the concrete cracking load. However, from the concrete cracking load up to the steel yielding load, the ($P-\delta$) curves obtained from the perfect bond FE models (either the conventional or the modified one) appeared to be stiffer than the experimental curve, this stiffness was slightly decreased when the CZM was employed. In the ultimate strength stage, i.e. from the steel yielding load to the failure load, the conventional PBM overestimated the stiffness and load-carrying capacity of the beam; this is because the PBM ignores the shear stress/strain between the CFRP/resin and concrete which mainly occur in this stage. On the other hand, the stiffness and load-carrying capacity values of the modified PBM (PBM,$\alpha = 0.7$) and CZM were considerably close to the experimental values. The predicted ultimate

load and deflection (P_u and δ_u) of beam BC1-N-NSM were within (9.8-0.19)%, (2.1-0.5)% and (0.1-0.2)% error band, respectively, for the PBM, modified PBM and CZM. For beam BC2-N-SNSM, the values of $P_u$and δ_u were within (15.6-11.4)%, (2.3-5.5)% and (0.7-5.2)%, error band, respectively, for the PBM, modified PBM and CZM. These results justify the reduction that was applied to the nominal tensile strength of the CFRP bars, as discussed in section 3.2.1, and validate the bond-slip law that was adopted to estimate behavior of the interface bond between the strengthening bars and concrete, as discussed in section 3.2.2.

It is worth mentioning that, although the modified PBM ($\alpha = 0.7$) is valid within the framework of this research, the great correspondence between the experimental and FE analysis results for the strengthened beams (BC1-E-NSM and BC2-E-SNSM) in terms of the ultimate load and deflection proves the accuracy of the experimental results, in particular the readings from the strain gauges, and the constitutive models used for modeling steel, concrete, CFRP and resin materials.

3.4.2 Cracks pattern and failure modes

Fig. 21 shows the cracking maps and failure modes of strengthened beams (BC1-N-NSM and BC2-N-SNSM) obtained from the FE analysis using the cohesive zone model (CZM). As can be seen from Fig.21, adopting the CFRP bars for strengthening continuous RC beams significantly increase the number of the cracks in the hogging and sagging regions, especially for the beam strengthened with side-NSM CFRP bars. The crack patterns observed from the experimental tests (Figs.5 and 7) and those from the numerical simulations were quite similar, which confirms that the CZM can successfully capture the mechanism of fracture in the beams.

In general, the prediction of the nonconventional failure modes, such as debonding/pull out of the CFRP bars using the FE analysis, is more complicated. The cohesive zone model proposed in this study, on the other hand, can still capture to some extent these failure modes, as illustrated in Fig.21, in which the red color represents the cracked elements that describe the mode of failure. As explained earlier, the proposed CZM was principally applied to exemplify the interaction between the strengthening components and concrete. Therefore, both of the FE beam models showed that failure occurred in the cohesive layer indicating debonding. The reported maximum FE shear stress/slip of the CFRP bar in the hogging region of beams BC1-E-NSM and BC2-E-SNSM were 5.96 MPa/6.01 mm and 5.55 MPa/5.38 mm, respectively.

3.4.3 Central support reaction and moment redistribution

The evolution of the actual central supports reactions gives an indication for redistribution of the moment in the statically indeterminate RC beams. Hence, Fig.22 presents the central support reaction of the tested beams obtained from the experimental and FE analysis results versus the total applied load at different load levels, along with a comparison of the elastic reactions which were computed by considering a uniform flexural stiffness throughout the entire length of the beam. From Fig.22, the great convergence between the experimental results and the FE analysis results is clear. For beams CB-N, BC1-N-NSM and BC2-N-

SNSM, the central support reaction at the ultimate load level were 110.2 kN, 180.9 kN and 167.1 kN, respectively, whereas the measured reactions from the tests at the same load level were 110.1 kN, 180.3 kN and 166.6 kN, respectively. Consequently, the computed moment redistribution degree (β) for the FE beam models were very close to those reported in Table2 (see also Tables 5-6).

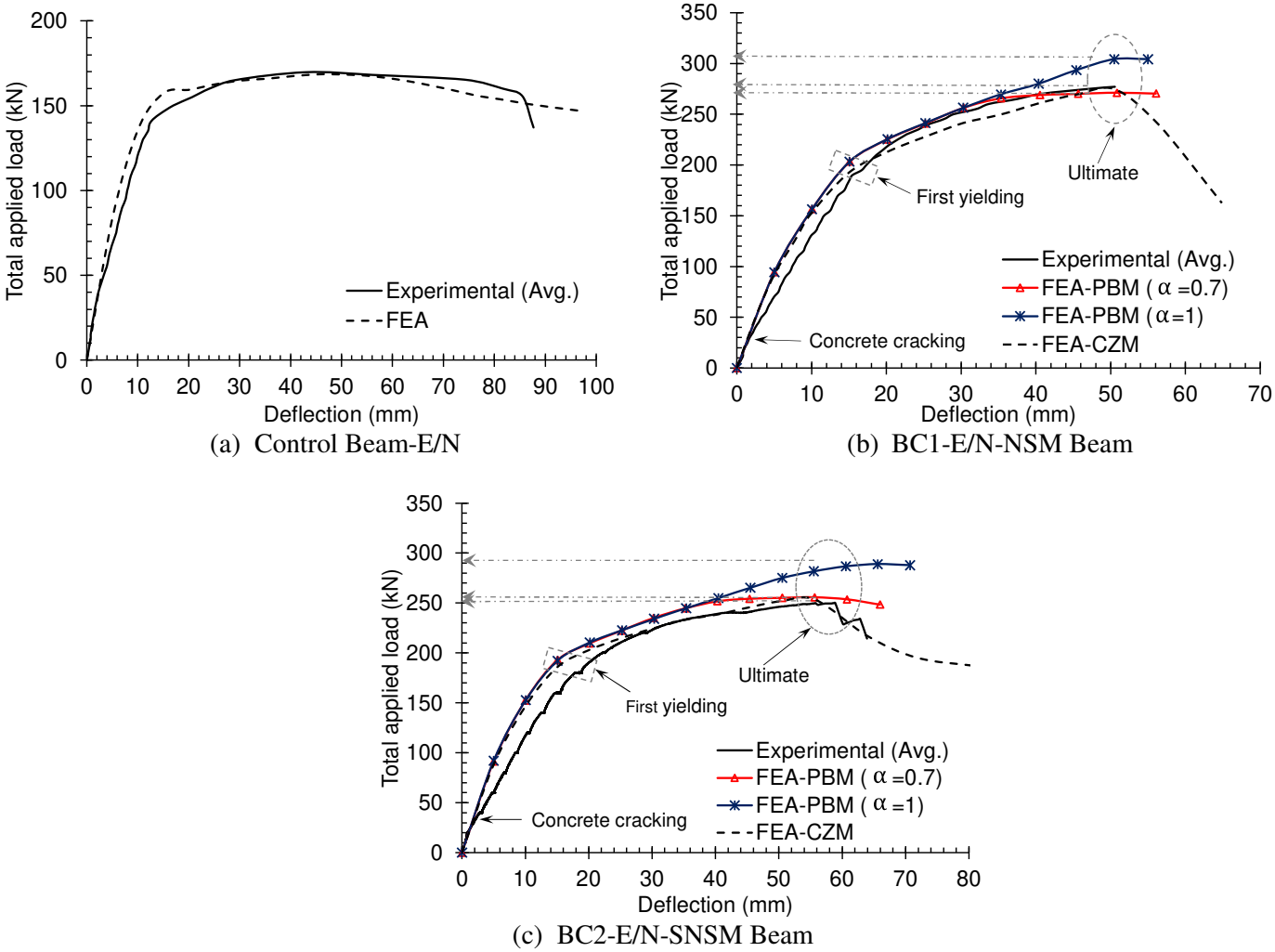

(a) Control Beam-E/N

(b) BC1-E/N-NSM Beam

(c) BC2-E/N-SNSM Beam

Fig. 20: The experimental and numerical load deflection curves of tested beams.

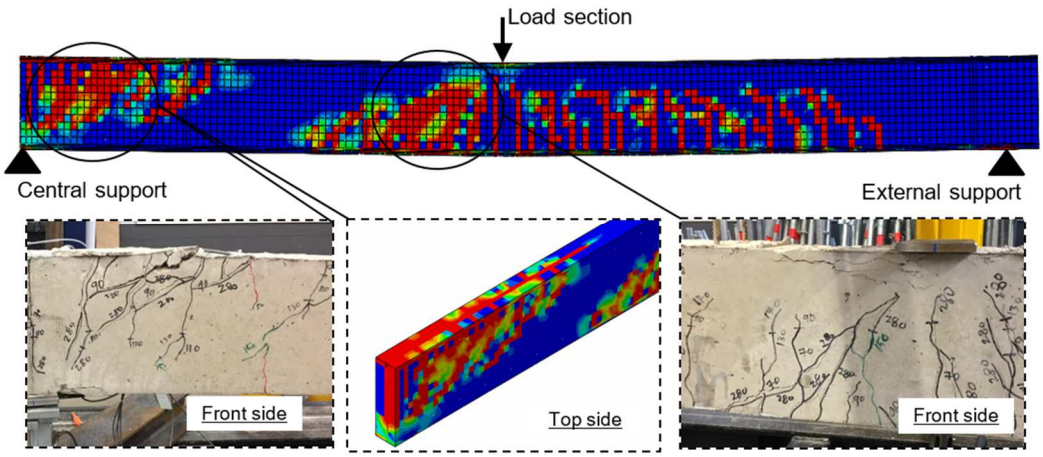

(a) BC1-N-NSM

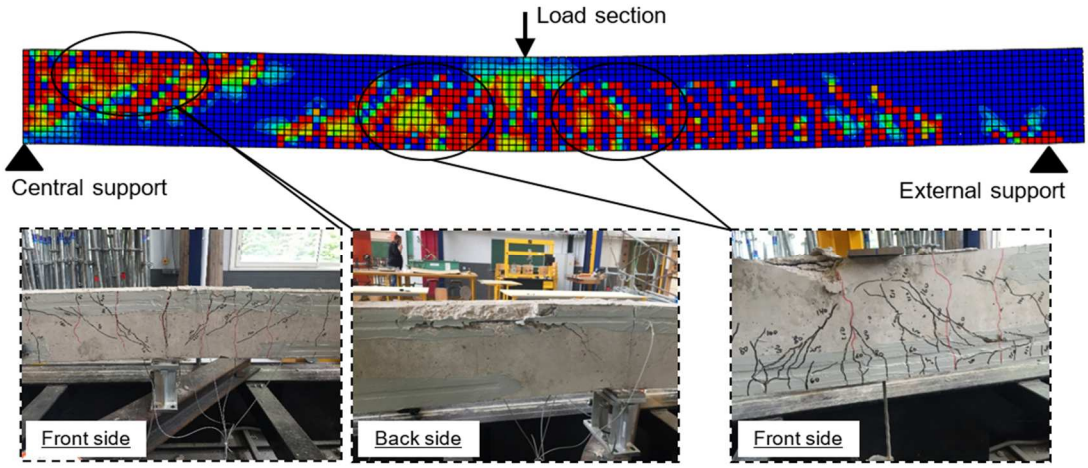

(b) BC2-N-SNSM

Fig. 21: Cracks maps and failure of strengthened beams

3.4.4 Effectiveness of the CFRP bars

As stated in the experimental sections of this paper (section 2.2.4), position of the strengthening was found to be slightly influence the effectiveness of the CFRP bars at the ultimate load level. Fig.23 presents the tensile stresses of the CFRP bars at the ultimate load in the strengthened beam specimens, as obtained from the FE analysis (CZM). The FE stresses corresponded well to the experimental stresses. The maximum tensile stress of the CFRP bars in both beams was reported in the hogging region; and the CFRP bars effectiveness ($\frac{\sigma_{max}^{CFRP}}{\sigma_{ult}^{CFRP}}$) was about 72% for beam BC1-N-NSM and about 68.8% for beam BC2-N-SNSM.

3.5 Parametric study-Arrangement of the reinforcement

Based on the above discussion, it can be asserted that the cohesive zone model (CZM) is

suitable for analyzing behavior of continuously reinforced concrete beams strengthened with CFRP bars by means the NSM and side-NSM techniques. The main parameters influencing the behavior of statically indeterminate RC beams are the amount and arrangement of the tension reinforcements. Consequently, the proposed CZM model is employed in this section for studying effects of these parameters on the load-carrying capacity and moment redistribution of strengthened continuous two-span RC beams.

The parametric study was conducted with distinct strengthening arrangements in the negative and positive moment regions of beams, as summarized in Tables 5a-c, where A_f^H and A_f^S are the area of CFRP bars in the hogging and sagging regions, respectively. The dimensions, positive steel reinforcement ratio (ρ_s^S=1%), load and support conditions of the FE beams were all similar to those used in the experimental program (Fig.1).

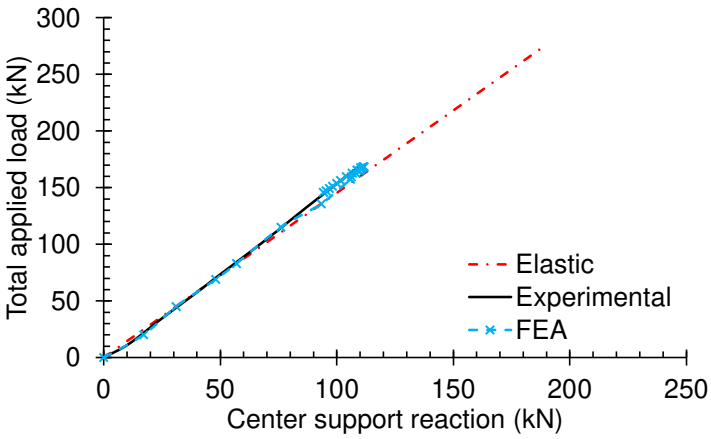

(a) Control Beam-E/N

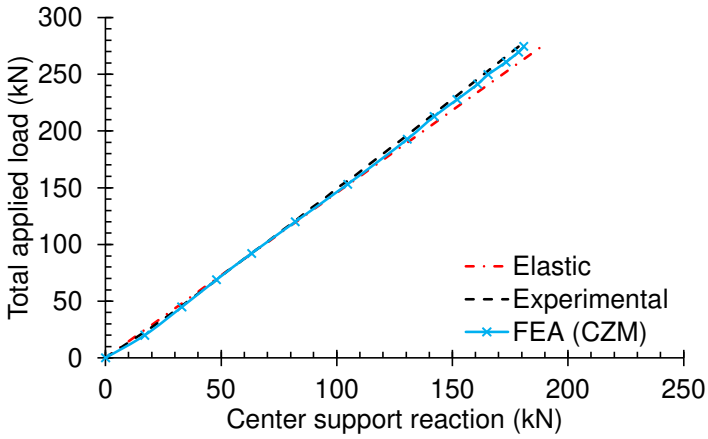

(b) BC1-E/N-NSM Beam

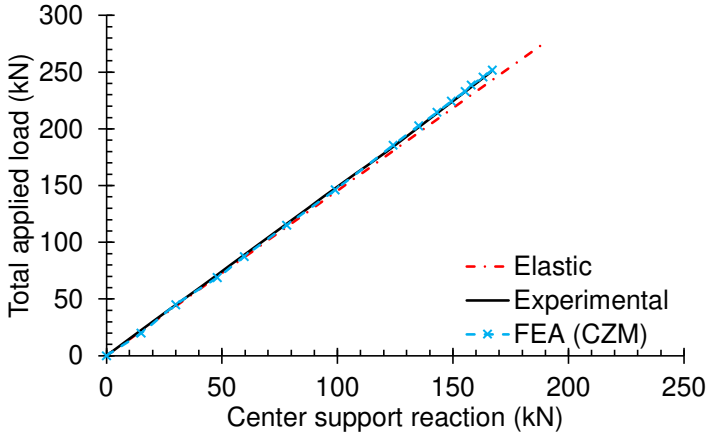

(c) BC2-E/N-SNSM Beam

Fig. 22: The experimental and FEA reults of central support reaction of tested beams

A total of 21 strengthened beams were investigated. The FE beam specimens had different steel reinforcement ratios in the hogging region, i.e. ρ_s^H = 0.5%, 1% and 1.25%. For each steel ratio, the applied strengthening arrangements were classified into three groups: a) The hogging region (x-0), b) The sagging region (0- x) and c) The hogging and sagging region (x

- x), where x refers to the number of CFRP bars.

In order to ensure the validation of the adopted cohesive zone model for studying the influences of the strengthening and reinforcement arrangement on the behavior of continuous RC beams, an additional beam namely BC1-N-NSM-(0-2) from Table 5b was also experimentally tested. This beam was strengthened with CFRP bars in the sagging regions only. The experimental load-deflection curve of this beam (BC1-N-NSM-(0-2)) is plotted in Fig.24, and its failure mode is presented in the Appendix.

Fig. 24 shows the load-deflection curves of all simulated beams, whereby it was easy to perceive the ductile failure of side-NSM beams compared to the NSM beams. Tables 6a, 6b and 6c summarize the FE results according to the different steel reinforcement ratios used in the hogging region. In Tables 6a-c, P_u and δ_u are respectively the ultimate load and deflection, R_c is the central reaction at the ultimate load level, β_H and β_S are respectively the moment redistribution degree in the hogging and sagging region; and λ is the load-carrying capacity index that is defined as the ratio of the ultimate load of the strengthened beam to that of the control beam. Two criteria were assumed to describe the failure modes obtained from the FE analysis: (i) The flexural failure (F), indicating yielding of the tension steel followed by concrete crushing; the concrete crushing was assumed to takes place when its compressive strain exceeds the value 0.003. (ii) The damage of the cohesive layer, indicating interfacial debonding failure (D).

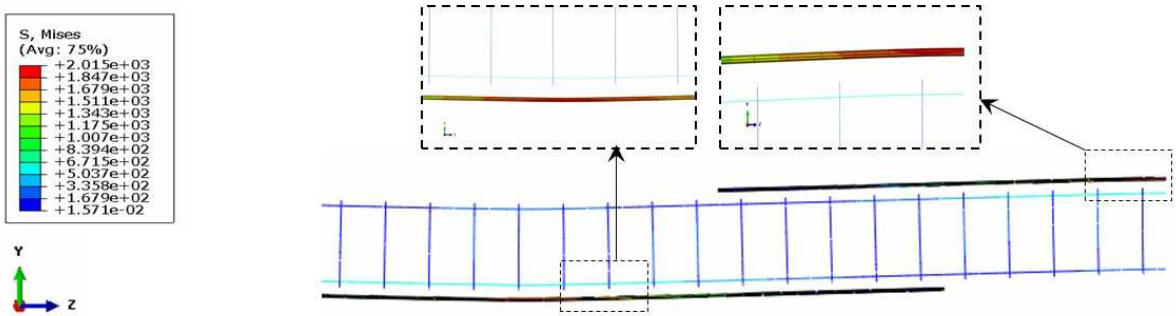

(a) BC1-N-NSM

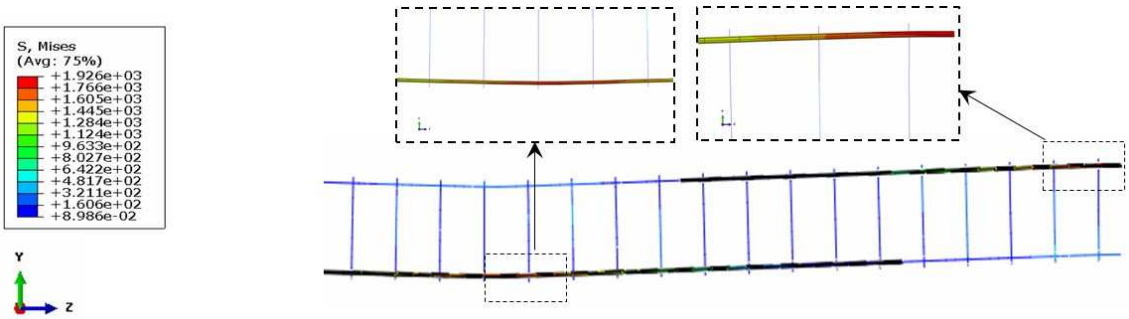

(b) BC2-N-SNSM

Fig. 23: The FEA (CZM) tensile stress of CFRP bars in the strengthened beams at the ultimate load level

Table 5-a. Resume of the strengthening arrangements, $\rho_s^H = 0.5\%$. (2D10)

Beam	Hogging region strengthening			Sagging region strengthening			A_f^H mm2	A_f^H/A_s^H (%)	A_f^S mm2	A_f^S/A_s^S (%)
	No.	Length	SL/BL	No.	Length	SL/BL				
Control Beam-N-(0-0)	----	----	----	----	----	----	0	0	0	0
BC1-N-NSM-(0-2)	----	----	----	2Ø6	2.3	0.65	0	0	56.5	18
BC1-N-NSM-(2-0)	2Ø6	2.0	0.70	----	----	----	56.5	36	0	0
BC1-N-NSM-(2-2)	2Ø6	2.0	0.70	2Ø6	2.3	0.65	56.5	36	56.5	18
BC2-N-SNSM-(0-2)	----	----	----	2Ø6	2.3	0.65	0	0	56.5	18
BC2-N-SNSM-(2-0)	2Ø6	2.0	0.70	----	----	----	56.5	36	0	0
BC2-N-SNSM-(2-2)	2Ø6	2.0	0.70	2Ø6	2.3	0.65	56.5	36	56.5	18

Table 5-b. Resume of the strengthening arrangements, $\rho_s^H = 1\%$, (2D14)

Beam	Hogging region strengthening			Sagging region strengthening			A_f^H mm2	A_f^H/A_s^H (%)	A_f^S mm2	A_f^S/A_s^S (%)
	No.	Length	SL/BL	No.	Length	SL/BL				
Control Beam-N-(0-0)	----	----	----	----	----	----	0	0	0	0
BC1-N-NSM-(0-2)	----	----	----	2Ø6	2.3	0.65	0	0	56.5	18
BC1-N-NSM-(2-0)	2Ø6	2.0	0.70	----	----	----	56.5	18	0	0
BC1-N-NSM-(2-2)	2Ø6	2.0	0.70	2Ø6	2.3	0.65	56.5	18	56.5	18
BC2-N-SNSM-(0-2)	----	----	----	2Ø6	2.3	0.65	0	0	56.5	18
BC2-N-SNSM-(2-0)	2Ø6	2.0	0.70	----	----	----	56.5	18	0	0
BC2-N-SNSM-(2-2)	2Ø6	2.0	0.70	2Ø6	2.3	0.65	56.5	18	56.5	18

Table 5-c. Resume of the strengthening arrangements, $\rho_s^H = 1.28\%$, (2D16)

Beam	Hogging region strengthening			Sagging region strengthening			A_f^H mm2	A_f^H/A_s^H (%)	A_f^S mm2	A_f^S/A_s^S (%)
	No.	Length	SL/BL	No.	Length	SL/BL				
Control Beam-N-(0-0)	----	----	----	----	----	----	0	0	0	0
BC1-NSM-N-(0-2)	----	----	----	2Ø6	2.3	0.65	0	0	56.5	18
BC1-NSM-N-(2-0)	2Ø6	2.0	0.70	----	----	----	56.5	14.1	0	0
BC1-NSM-N-(2-2)	2Ø6	2.0	0.70	2Ø6	2.3	0.65	56.5	14.1	56.5	18
BC2-SNSM-N-(0-2)	----	----	----	2Ø6	2.3	0.65	0	0	56.5	18
BC2-SNSM-N-(2-0)	2Ø6	2.0	0.70	----	----	----	56.5	14.1	0	0
BC2-SNSM-N-(2-2)	2Ø6	2.0	0.70	2Ø6	2.3	0.65	56.5	14.1	56.5	18

Table 6.a. FEA results of the strengthening arrangements, $\rho_s^H = 0.5\%$. (2D10)

Beam	P_u	δ_u	λ	R_c	β_H	β_S	σ_{CFRP}^{max}	$\sigma_{CFRP}^{max}/\sigma_{CFRP}^{ult}$	Shear stress*		Failure mode
									H	S	
CB-N-(0-0)	143.5	40.4	1	86.8	49.6	-28.8	----	----	----	----	F
BC1-N-NSM-(0-2)	199.1	47.4	1.39	116.1	55.7	-33.4	1783	0.64	----	5.96	D in S
BC1-N-NSM-(2-0)	185.1	55.9	1.29	124.7	7.4	-4.4	2156	0.77	4.95	----	F
BC1-N-NSM-(2-2)	227.8	47.3	1.59	147.1	22.3	-12.6	2158	0.77	5.82	5.96	D in S and H
BC2-N-SNSM-(0-2)	202.8	55.7	1.41	117.5	57.7	-34.6	1796	0.64	----	4.44	F
BC2-N-SNSM-(2-0)	185	63.6	1.29	118.7	24.5	-14.7	1877	0.67	4.11	----	F
BC2-N-SNSM-(2-2)	230.5	55.7	1.61	144	33.5	-20.1	2020	0.72	5.12	4.33	F

F: flexural; D: debonding; S: sagging and H: hogging. *Maximum shear stress induced in the cohesive zone

Table 6.b. FEA results of the strengthening arrangements, $\rho_s^H = 1\%$, (2D14)

Beam	P_u	δ_u	λ	R_c	β_H	β_S	σ_{CFRP}^{max}	$\sigma_{CFRP}^{max}/\sigma_{CFRP}^{ult}$	Shear stress*		Failure mode
									H	S	
CB-N-(0-0)	169.5	45.6	1	110.2	20.1	-12	----	----	----	----	F
BC1-NSM-N-(0-2)	227.9	47.3	1.34	142.4	33.6	-20.1	1886	0.67	----	5.91	D in S
BC1-NSM-N-(2-0)	202.3	55.6	1.19	143.3	-10.8	6.7	1981	0.71	4.51	----	F
BC1-NSM-N-(2-2)	277.5	50.5	1.64	180.9	19	-11.3	2015	0.72	5.96	5.73	D in H
BC2-SNSM-N-(0-2)	231.4	55.8	1.37	144.1	34.5	-20.7	1867	0.67	----	5.08	F
BC2-SNSM-N-(2-0)	214.2	63.8	1.26	147.5	-0.6	0.4	2135	0.76	4.58	----	F
BC2-SNSM-N-(2-2)	251.8	55.8	1.49	167.1	12.9	-7.6	1926	0.69	5.55	5.84	D in S and H

F: flexural; D: debonding; S: sagging and H: hogging. *Maximum shear stress induced in the cohesive zone

Table 6.c. FEA results of the strengthening arrangements, $\rho_s^H = 1.28\%$, (2D16

Beam	P_u	δ_u	λ	R_c	β_H	β_S	σ_{CFRP}^{max}	$\sigma_{CFRP}^{max}/\sigma_{CFRP}^{ult}$	Shear stress*		Failure mode
									H	S	
CB-N-(0-0)	183.9	55.7	1	126.9	-1.4	0.8	----	----	----	----	F
BC1-NSM-N-(0-2)	242.3	47.4	1.32	156	23.3	-14	1887	0.67	----	5.23	F
BC1-NSM-N-(2-0)	217.7	56	1.18	158.3	-21.1	12.7	2025	0.72	4.95	----	F
BC1-NSM-N-(2-2)	281.1	56	1.53	191.7	2.9	-1.8	2128	0.76	5.57	5.91	D in S
BC2-SNSM-N-(0-2)	244.1	55.8	1.33	157.2	23.2	-13.9	1897	0.68	----	4.86	F
BC2-SNSM-N-(2-0)	226.6	63.9	1.23	160.1	-10.2	6.1	2031	0.72	4.96	----	F
BC2-SNSM-N-(2-2)	269.3	56.9	1.46	181.8	6.6	-4	1964	0.70	5.10	5.02	F

F: flexural; D: debonding; S: sagging and H: hogging. *Maximum shear stress induced in the cohesive zone

The FE analysis results indicated in Tables 6a-c can point out the following observations:

I. The arrangement of the CFRP and amount of the steel reinforcement had significant effects on the moment redistribution of continuous RC beams, and they can even change the direction of redistribution.

II. The increase in the steel reinforcement ratio in the hogging region (ρ_s^H) caused a decrease in the positive moment redistribution of continuous RC beams, regardless of the strengthening technique used. However, for beams reinforced with the same ρ_s^H, strengthening only the sagging moment regions was found to increase the moment redistribution. This can be explained by the fact that the flexural stiffness of the sagging region was greater than that of the hogging region.

III. According to the moment redistribution capability at the ultimate state for beams strengthened in the hogging moment regions only, it was found that using the side-NSM CFRP bars slightly decreased stiffness of the hogging region in comparison with the NSM CFRP bars.

IV. Applying the CFRP bars in both hogging and sagging regions of the beam was found the most effective strengthening arrangement of the CFRP bars in order to improve the beam's load-carrying capacity. Compared to the control beam specimens, the ultimate load of beam BC1-N-NSM-(2-2) was improved by about 59%, 64% and 53% for ρ_s^H = 0.5%, 1% and 1.28%, respectively. Similarly, the ultimate load of beam BC2-N-SNSM-(2-2) was improved by about 61%, 49% and 46% for ρ_s^H = 0.5%, 1% and 1.28%, respectively.

V. The side-NSM technique was relatively more efficient than the bottom/top NSM technique when the CFRP bars were applied only in the hogging region or the sagging region. For example, for a reinforcement ratio of 1%, the value of λ was found equal to 19% and 34%, for NSM beams (BC1-NSM-(2-0) and BC1-NSM-(0-2)), and 26% and 37%, for side-NSM beams (BC2-SNSM-(2-0) and BC2-SNSM-(0-2)).

VI. The contribution of CFRP bars to the load-carrying capacity of the beams was limited by the occurrence of concrete crushing or by the damaged strengthening system. It was also observed that the utilization level of the CFRP bars ($\sigma_{CFRP}^{max}/\sigma_{CFRP}^{ult}$) at the ultimate load ranged from 64% to 77%, which justifies the relatively low influence of the steel reinforcement ratio (ρ_s^H), strengthening arrangement and strengthening position on the effectiveness of the CFRP bars.

4. Conclusion

The present study aimed to analyze the global flexural response of statically indeterminate RC beams strengthened with CFRP rods using the NSM and side-NSM techniques. According to the obtained results, the following conclusions could be drawn:

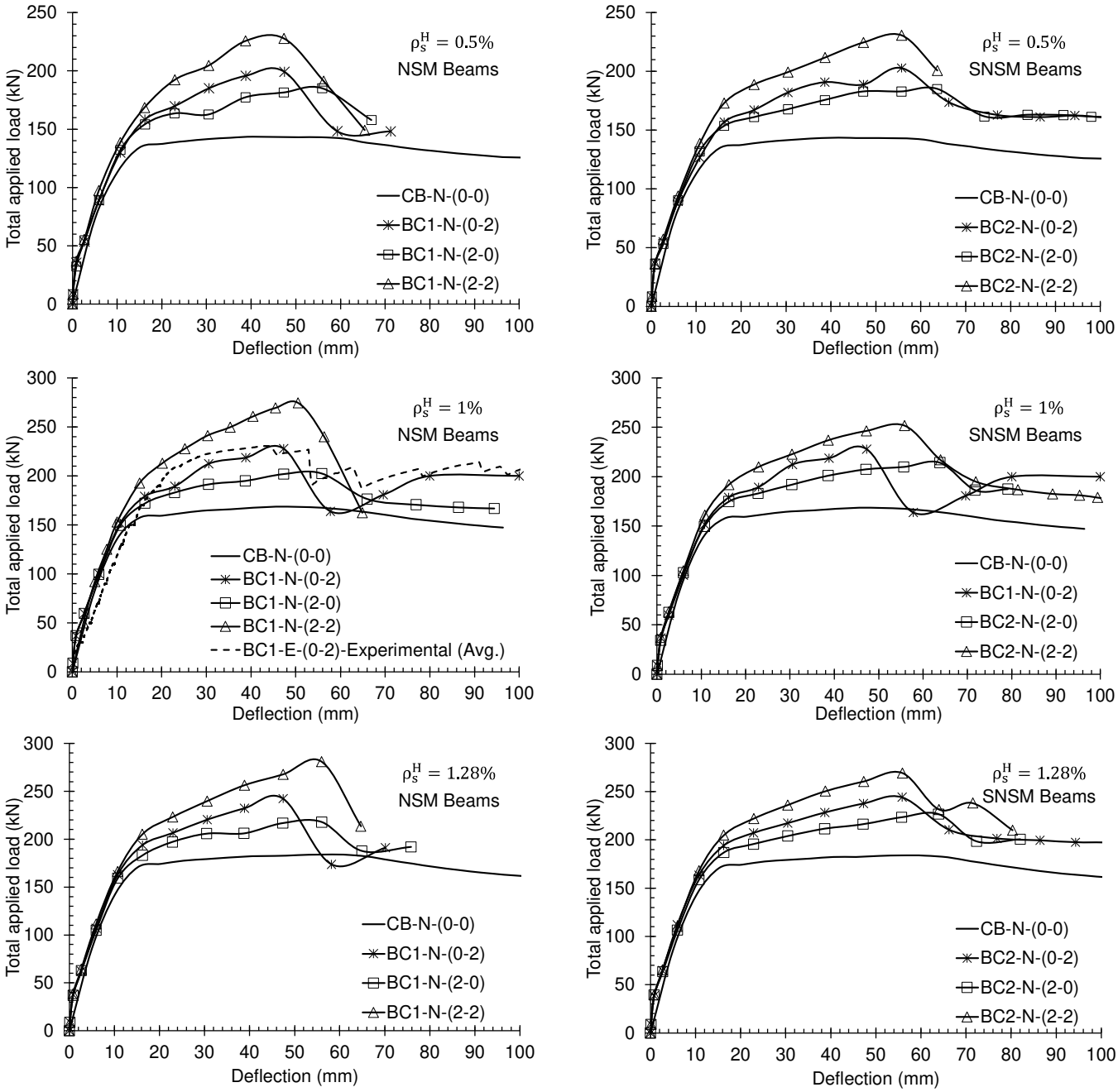

Fig.24.Load-deflection curves of FE beams

- All strengthened continuous RC beam either tested or FE modeled using the NSM and side-NSM CFRP bars techniques exhibited improvement in their load carrying capacity with respect to that of the un-strengthened beams, regardless of the CFRP arrangement or steel reinforcement ratio used. The highest increase of beam's load-

carrying capacity (λ) was achieved when the strengthening configuration composed CFRP bars in both hogging and sagging regions. However, when a relatively low steel reinforcement ratio was employed in the hogging region ($\rho_s^H = 0.5\%$), this strengthening configuration showed a slightly lower load-carrying capacity of the side-NSM beams in comparison with the NSM beams. This difference increased to about 10% when the hogging's steel ratio was raised to 1% and 1.28%.

- For all the strengthening configurations adopted in this research study, the increase of load-carrying capacity (λ) of beams strengthened with NSM-CFRP bars varied between 18% and 64%, whereas an increase in λ between 23% and 61%, was registered for beams strengthened with side-NSM-CFRP bars.
- In comparison with the NSM-CFRP bars technique, insertion of CFRP bars in the lateral sides adjacent to the steel bars using the side-NSM technique proved to considerably increase the number of cracks in the hogging and sagging regions. However, with the both strengthening techniques, the crack widths of beams were almost identical under the same applied load.
- The moment redistribution degree (β) of strengthened RC beams decreased as the steel reinforcement amount in the hogging region increased. In addition, the experimental and finite element results showed that the β was significantly affected by the position and arrangement of the CFRP bars.
- The three-dimensional finite element analysis developed with the cohesive zone bond model, presented in this study, can capture the main aspects observed from the experiments, for both NSM and side-NSM beams, regarding the load-carrying capacity, cracks pattern, effectiveness of the CFRP bars and the beam's moment redistribution.

Acknowledgments

The authors acknowledge the financial support of the Freyssinet Company, France.

Appendix

(a) Central support (b) Left span (c) Right span

Fig.A.1: Failure mode of beam BC1-E-NSM-(0-2)

References

[1] De Lorenzis L., J.G. Teng. Near-surface mounted FRP reinforcement: an emerging technique for strengthening structures, Compos Part B-Eng, 38 (2007), 119–143. https://doi.org/10.1016/j.compositesb.2006.08.003.

[2] Khalifa A.M.. Flexural performance of RC beams strengthened with near surface mounted CFRP strips. Alexandria Eng J, 55(2016):1497–1505.https://doi.org/10.1016/j.aej.2016.01.033.

[3] Ayesha Siddika, Md. Abdullah Al Mamun, Rayed Alyousef, Y.H. Mugahed Amran. Strengthening of reinforced concrete beams by using fiber-reinforcedpolymer composites: A review. Journal of Building Engineering 25 (2019) 100798.

[4] Salam Al-Obaidi, Yasir M. Saeed, Franz N. Rad, Flexural strengthening of reinforced concrete beams with NSM-CFRP bars using mechanical interlocking Journal of Building Engineering, 31 (2020) 101422. https://doi.org/10.1016/j.jobe.2020.101422

[5] MdAkter Hosen , MohdZamin Jumaat , Belal Alsubari , N. H. Ramli Sulong, d , Zainah Ibrahim , U. Johnson Alengaram , Huzaifa Hashim. Effect of bonding materials on the flexural improvement in RC beams strengthened with SNSM technique using GFRP bars. Journal of Building Engineering 32 (2020) 101777. https://doi.org/10.1016/j.jobe.2020.101777

[6] Al-Mahmoud F., A. Castel, R. François, C. Tourneur. Strengthening of RC members with near-surface mounted CFRP rods, Composite Structures, 91(2009), 138-147. https://doi.org/10.1016/j.compstruct.2009.04.040.

[7] Al-Mahmoud F., A. Castel, R. François. Failure modes and failure mechanisms of RC members strengthened by NSM CFRP composites – analysis of pull-out failure mode, Composites Part B: Engineering,43(2012), 1893-1901. https://doi.org/10.1016/j.compositesb.2012.01.020.

[8] Dias S.J.E., J.A.O. Barros, W. Janwaen. Behavior of RC beams flexurally strengthened with NSM CFRP laminates, Composite Structures, 201(2018), 363-376. https://doi.org/10.1016/j.compstruct.2018.05.126.

[9] Almassri B., F. Al Mahmoud, R. Francois. Behaviour of corroded reinforced concrete beams repaired with NSM CFRP rods, experimental and finite element study. Composites Part B, 92 (2016), 477-488. https://doi.org/10.1016/j.compositesb.2015.01.022

[10] Sharaky I.A., M. Baena, C. Barris, H.E.M. Sallam, L. Torres. Effect of axial stiffness of NSM FRP reinforcement and concrete cover confinement on flexural behaviour of strengthened RC beams: Experimental and numerical study. Engineering Structures 173 (2018), 987–1001. https://doi.org/10.1016/j.engstruct.2018.07.062

[11] Ferracuti B., M. Savoia, C. Mazzotti. A numerical model for FRP–concrete delamination. Composites Part B: Engineering, 37(2006), 356-364. https://doi.org/10.1016/j.compositesb.2005.08.002.

[12] Chen G, J Teng, J Chen. Finite-element modeling of intermediate crack debonding in FRP-plated RC beams. Journal of Composites for Construction, 15(2011), 339–53. https://doi.org/10.1061/(ASCE)CC.1943-5614.0000157.

[13] Arruda M.R.T., J.P. Firmo, J.R. Correia, C. Tiago. Numerical modelling of the bond between concrete and CFRP laminates at elevated temperatures, Engineering Structures, 110 (2016), 233-243. https://doi.org/10.1016/j.engstruct.2015.11.036.

[14]Amir Shomali, Davood Mostofinejad, Mohammad Reza Esfahani. Experimental and numerical investigation of shear performance of RC beams strengthened with FRP using grooving method. Journal of Building Engineering 31 (2020) 101409

[15] Abdallah M., F. Al Mahmoud , R. Boissière , A. Khelil , J. Mercier. Experimental study on strengthening of RC beams with Side Near Surface Mounted technique-CFRP bars. Composite Structures 234 (2020) 111716. https://doi.org/10.1016/j.compstruct.2019.111716.
[16] Rami H. Haddad, Emad M. Yaghmour. Side NSM CFRP strips with different profiles for strengthening reinforced concrete beams. Journal of Building Engineering 32 (2020) 101772.
[17] Abdallah M., F. Al Mahmoud, A. Khelil, J. Mercier, B. Almassri. Assessment of the flexural behavior of continuous RC beams strengthened with NSM-FRP bars, experimental and analytical study, Composite Structures, 242 (2020) 112127. https://doi.org/10.1016/j.compstruct.2020.112127.
[18] ABAQUS version 6.13, 2013. Computer software, Assault Systems, Waltham. MA.
[19] ACI Committee 440. Guide For The Design And Construction Of Externally Bonded FRP Systems For Strengthening Concrete Structures. American Concrete Institute, 2017, Farmington Hills, MI., USA.
[20] AL-Mahmoud F., A. Castel, R. Franc¸ois, C. Tourneur. Effect of surface pre-conditioning on bond of carbon fibre reinforced polymer rods to concrete, Cement & Concrete Composites, 29(2007), 677-689. https://doi.org/10.1016/j.cemconcomp.2007.04.010.
[21] Hassan T. and S. Rizkalla. Investigation of Bond in Concrete Structures Strengthened with Near Surface Mounted CFRP Strips, Journal of Composites for Construction ASCE, 7 (2003), 248-257. https://doi.org/10.1061/(ASCE)1090-0268(2003)7:3(248).
[22] De Lorenzis L.; K. Lundgren; and A. Rizzo. Anchorage Length of Near-Surface-Mounted FRP Bars for Concrete Strengthening—Experimental Investigation and Numerical Modeling, ACI Structural Journal, 101 (2004), 269-278. DOI:10.14359/13025
[23] Tahnat Y.B.A., M.M.S. Dwaikat, M.A. Samaaneh. Effect of using CFRP wraps on the strength and ductility behaviors of exterior reinforced concrete joint. Composite Structures, 201 (2018), 721–739. https://doi.org/10.1016/j.compstruct.2018.06.082.
[24] Algaard W., J. Lyle, C. Izzat. Perforation of composite floor. 5th European LS-DYNA Users Conference, 2005, Birmingham, UK, May.
[25] Nguyen H.T., S. E. Kim. Finite element modeling of push-out tests for large stud shear connectors, Journal of Constructional Steel Research, 65(2009), 1909-1920. https://doi.org/10.1016/j.jcsr.2009.06.010.
[26] ABAQUS, 2013, ABAQUS Analysis User's Manual Version 6.13, Assault Systems.
[27] Omran H.Y., R. El-Hacha. Nonlinear 3D finite element modeling of RC beams strengthened with prestressed NSM-CFRP strips, Construction and Building Materials, 31(2012), 74–85. https://doi.org/10.1016/j.conbuildmat.2011.12.054.
[28] Lubliner J., J. Oliver, S. Oller , E. Oñate. A plastic-damage model for concrete, Int. J. Solids Structures. 25(1989), 229–326. https://doi.org/10.1016/0020-7683(89)90050-4.
[29] Lee J., G.L. Fenves, Plactic-damage model for cyclic loading of concrete structures, Journal of Engineering Mechanics, 124 (1998), 892–900. https://doi.org/10.1061/(ASCE)0733-9399(1998)124:8(892).
[30] Bezerra L.M., O.O. Cavalcante, L. Chater, J. Bonilla. V-shaped shear connector for composite steel-concrete beam, Journal of Constructional Steel Research, 150(2018), 162-174. https://doi.org/10.1016/j.jcsr.2018.07.016 .
[31] Wahalathantri B.L., D.P. Thambiratnam, T.H.T. Chan, S. Fawzia. A material model for flexural crack simulation in reinforced concrete elements using ABAQUS. First International conference on engineering, designing and developing the built environment for sustainable wellbeing, 2011, Brisbane, Australia, April.
[32] Alfarah B., F. López-Almansa, S. Oller. New methodology for calculating damage variables evolution in plastic damage model for RC structures, Engineering Structures. 132 (2017),

70–86. https://doi.org/10.1016/j.engstruct.2016.11.022.
[33] Rezazadeh M., I. Costa, J. Barros. Influence of prestress level on NSM CFRP laminates for the flexural strengthening of RC beams, Composite Structures, 116(2014), 489-500. https://doi.org/10.1016/j.compstruct.2014.05.043.
[34] Abouali S., M. Shahverdia, M. Ghassemieh, M. Motavallia. Nonlinear simulation of reinforced concrete beams retrofitted by nearsurface mounted iron-based shape memory alloys, Engineering Structures, 187(2019), 133–148. https://doi.org/10.1016/j.engstruct.2019.02.060.
[35] Hawileh R.A.. Nonlinear finite element modeling of RC beams strengthened with NSM FRP rods, Construction and Building Materials, 27(2012), 461–471. https://doi.org/10.1016/j.conbuildmat.2011.07.018.
[36] Al-Mahmoud F ., A. Castel, R. François, C. Tourneur. Anchorage and tension stiffening effect between Near-Surface-Mounted carbon fiber reinforcement polymer rods and concrete, Cement and Concrete Composites, 33(2011), 346–52. https://doi.org/10.1016/j.cemconcomp.2010.10.016.
[37] Capozucca R.. Analysis of bond-slip effects in RC beams strengthened with NSM CFRP rods, Composite Structures, 102(2013), 110–123. https://doi.org/10.1016/j.compstruct.2013.02.024.
[38] Seracino R., M.M.R. Saifulnaz, D.J. Oehlers . Generic debonding resistance of EB and NSM plate-to-concrete joints, Journal of Composites for Construction, 11(2007), 62–70. https://doi.org/10.1061/(ASCE)1090-0268(2007)11:1(62).
[39] Obaidat Y.T., S. Heyden, O. Dahlblom. The effect of CFRP and CFRP/concrete interface models when modeling retrofitted RC beams with FEM. Composite Structures, 92(2010), 1391–1398. https://doi.org/10.1016/j.compstruct.2009.11.008.